

Review

Trends in Performance Limits of the HOT Infrared Photodetectors

Antoni Rogalski ¹, **Piotr Martyniuk** ^{1,*}, **Małgorzata Kopytko** ¹ and **Weida Hu** ²

¹ Faculty of Advanced Technologies and Chemistry, Institute of Applied Physics, Military University of Technology, 2 Kaliskiego St., 00-908 Warsaw, Poland; antoni.rogalski@wat.edu.pl (A.R.); malgorzata.kopytko@wat.edu.pl (M.K.)

² State Key Laboratory of Infrared Physics, Shanghai Institute of Technical Physics, Chinese Academy of Sciences, 500 Yu Tian Road, Shanghai 200083, China; wdhu@mail.sitp.ac.cn

* Correspondence: piotr.martyniuk@wat.edu.pl; Tel.: +48-26-183-92-15

Abstract: The cryogenic cooling of infrared (IR) photon detectors optimized for the mid- (MWIR, 3–5 μm) and long wavelength (LWIR, 8–14 μm) range is required to reach high performance. This is a major obstacle for more extensive use of IR technology. Focal plane arrays (FPAs) based on thermal detectors are presently used in staring thermal imagers operating at room temperature. However, their performance is modest; thermal detectors exhibit slow response, and the multispectral detection is difficult to reach. Initial efforts to develop high operating temperature (HOT) photodetectors were focused on HgCdTe photoconductors and photoelectromagnetic detectors. The technological efforts have been lately directed on advanced heterojunction photovoltaic HgCdTe detectors. This paper presents the several approaches to increase the photon-detectors room-temperature performance. Various kinds of materials are considered: HgCdTe, type-II A^{III}B^V superlattices, two-dimensional materials and colloidal quantum dots.

Keywords: HOT IR detectors; HgCdTe; P-i-N; BLIP condition; 2D material photodetectors; colloidal quantum dot photodetectors



Citation: Rogalski, A.; Martyniuk, P.; Kopytko, M.; Hu, W. Trends in Performance Limits of the HOT Infrared Photodetectors. *Appl. Sci.* **2021**, *11*, 501. <https://doi.org/10.3390/app11020501>

Received: 30 October 2020

Accepted: 14 December 2020

Published: 6 January 2021

Publisher's Note: MDPI stays neutral with regard to jurisdictional claims in published maps and institutional affiliations.



Copyright: © 2021 by the authors. Licensee MDPI, Basel, Switzerland. This article is an open access article distributed under the terms and conditions of the Creative Commons Attribution (CC BY) license (<https://creativecommons.org/licenses/by/4.0/>).

1. Introduction

HgCdTe takes the dominant position in infrared (IR) detector technology. This material has triggered the rapid development of the three “detector generations” considered for military and civilian applications and briefly described in the caption of Figure 1. IR detector technology combined with fabrication of epitaxial heterostructure [by molecular beam epitaxy (MBE) and metalorganic chemical vapor deposition (MOCVD)] and photolithographic processes revolutionized the semiconductor industry, thus enabling the design and fabrication of complex focal plane arrays (FPAs). Further their development will relate to implementation of fourth generation staring systems, which the main features are to be: high resolution (pixels $> 10^8$), multi-band detection, three-dimensional readout integration circuits (3D ROIC), and other integration functions such as polarization/phase sensitivity, better radiation/pixel coupling or avalanche multiplication. The first three generations of imaging systems primarily rely on planar FPAs. Several approaches to circumvent these limitations, including bonding the detectors to flexible or curved molds, have been proposed [1]. Evolution of fourth generation is inspired by the most famous visual systems, which are the biological eyes. Solution based on the Petzval-matched curvature allows the reduction of field curvature aberration. In addition, it combines such advantages as simplified lens system, electronic eye systems and wide field-of-view (FOV) [2,3]. The colloidal quantum dot (CQD) [4] and 2D layered material [5] photodetectors fabricated on flexible substrates exhibit the potential to circumvent technical challenges in the development of the fourth generation IR systems.

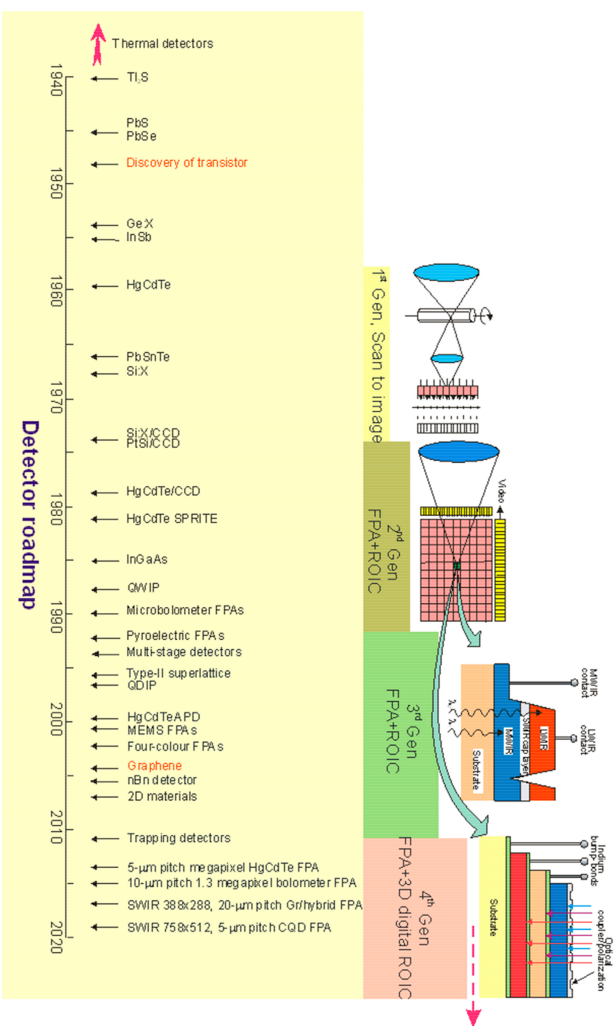


Figure 1. The history of IR detectors and systems development. Four generation systems for military and civilian applications can be considered: first generation (scanning systems), second generation (staring systems—electronically scanned), third generation (staring systems with large number of pixels and two-color functionality), and fourth generation (staring systems with very large number of pixels, multi-color functionality, 3D ROIC, and other on-chip functions; e.g., better radiation/pixel coupling, avalanche multiplication in pixels, polarization/phase sensitivity).

The need for cooling considerably limits more widespread use of IR technology. There are significant attempts to decrease system size, weight, and power consumption (SWaP) to limit IR system's cost and to increase the operating temperature. The invention of microbolometer array was a milestone step in development of IR cameras operating at 300 K. However, microbolometers belong to the class of thermal detectors with limited response time—typically in millisecond range and could not be used in the multiband applications. To omit this limitation, further efforts are directed to increase operating temperature of photon detectors.

Initial efforts in development of the high operating temperatures (HOT) photodetectors were focused on HgCdTe photoconductors and photoelectromagnetic detectors [6]. Many concepts have been implemented and tested to improve the performance of IR photodetectors operating at near 300 K and compiled in References [7–10]. In addition to photoresistors and photodiodes, three other types of IR detectors can operate at near 300 K: magnetic concentration detectors, photoelectromagnetic (or PEM) detectors and Demeter effect detectors. The HgCdTe non-equilibrium devices such as the Auger suppressed excluded photoconductors and extracted photodiodes require significant bias what creates excessive 1/f noise.

Up till now, mainly HgCdTe and Sb-based III-V ternary alloys including barrier detectors with type-II superlattices (T2SLs: InAs/GaSb and InAs/InAsSb) have been considered for HOT IR photodetectors. The recently published monograph covers this topic for III-V material systems [11]. In the past decade considerable progress in development of interband quantum cascade infrared photodetectors (IB QCIP) based on T2SLs, 2D material [12] and CQD photodetectors brought their performance close to commercial ones [13].

In 1999 Elliott et al. claimed that there is no fundamental obstacle to reach 300 K operation of photon detectors with background-limited performance even in reduced fields of view [14]. In this paper we attempt to reconsider the performance of different material systems for the HOT detection operation in IR spectral range. Theoretical estimates are collated with experimental data for different photodetectors.

2. Trends in Development of Infrared HOT Photodetectors

As is shown by Piotrowski and Rogalski [15], the IR detectors performance is limited by statistical character of generation-recombination processes in the material. Thermal processes in the device material limit the detectivity, D^* of an optimized IR detector. It can be given by the following equation

$$D^* = k \frac{\lambda}{hc} \left(\frac{\alpha}{G} \right)^{1/2}, \quad (1)$$

where λ —Wavelength, h —Planck's constant, c —Light speed, α —Absorption coefficient, G —Thermal generation in the active detector's region, k —Coefficient depending on radiation coupling to the detector. α/G is the absorption coefficient to the thermal generation rate ratio and can be considered as the fundamental figure of merit of any material used for IR detectors (α/G ratio could be used to evaluate any material). Among different bulk materials, the narrow gap semiconductors are more suitable for the HOT photodetectors than competitive technologies, such as extrinsic devices, Schottky barrier photodiodes, quantum dot infrared photodetectors (QDIP) and quantum well infrared photodetectors (QWIP) [16]. The high performance of intrinsic photodetectors results from high density of states in the conduction and valence bands (contributing to high IR absorption), and long carrier lifetime (contributing to low thermal generation).

The goal of IR detector technology is the fabrication of HOT photodetector characterized by the dark current lower than the background flux current and $1/f$ noise negligibly lower than to the background flux shot noise [17,18].

In several papers, it was shown that the detector size, d , and F-number ($f/#$) are the main IR systems parameters [19,20]. Since they depend on $F\lambda/d$ (λ —Wavelength), both influence the detection/identification range, as well as the noise equivalent difference temperature (NEDT) [20]

$$\text{Range} = \frac{D\Delta x}{M\lambda} \left(\frac{F\lambda}{d} \right), \quad (2)$$

$$\text{NEDT} \approx \frac{2}{C\lambda(\eta\Phi_B^{2\pi}\tau_{int})} \left(\frac{F\lambda}{d} \right), \quad (3)$$

where D —Aperture, M —Needed number of pixels to identify a target Δx , C —Scene contrast, η —Quantum efficiency (QE), $\Phi_B^{2\pi}$ —Background flux into a 2π FOV, τ_{int} —Integration time. According to the relations (2) and (3), the $F\lambda/d$ parameter could be used for IR system optimization. For the $f/1$ optics, the smallest practicable detector size should be $\sim 2 \mu\text{m}$ for the MWIR and $\sim 5 \mu\text{m}$ for the LWIR, respectively [21]. With more realistic $f/1.2$ optics, the smallest practicable detector size is $\sim 3 \mu\text{m}$ and $\sim 6 \mu\text{m}$ for the MWIR and LWIR, respectively.

Kinch claims that the IR system ultimate cost reduction could only be reached by the 300 K operation of depletion-current limited arrays with pixel densities that are fully consistent with background and diffraction-limited performance due to the system optics [20]. The depletion-current limited P-i-N photodiodes demand long Shockley-Read-Hall (SRH)

carrier lifetime, marked as τ_{SRH} , to meet the requirements of a low dark current. The long HgCdTe SRH lifetime makes this material a great candidate for 300 K condition [20].

3. The Ultimate HgCdTe Photodiode Performance

In 2007, the Teledyne Technologies published an empirical expression, called “Rule 07”, for estimation of the P-on-n HgCdTe photodiodes dark current versus normalized wavelength-temperature product ($\lambda_c T$) [22]. This metric is closely related to Auger 1 diffusion-limited photodiode with n-type active region doping concentration $\sim 10^{15} \text{ cm}^{-3}$. In the past decade, the Rule 07 has become very popular as a reference level for the other technologies (especially to III-V barrier and T2SLs devices). However, at present stage of technology, the fully depleted background limited HgCdTe photodiodes can reach the level of 300 K dark current considerably lower than predicted by the Rule 07. The discussion below explains exactly this statement.

3.1. SRH Carrier Lifetime

The SRH generation-recombination mechanism determines the carrier lifetimes in both lightly doped n- and p-type HgCdTe in which SRH centres are related to residual impurities and native defects. Kinch et al. in 2005 [23] published that the experimental carrier lifetimes for n-type LWIR HgCdTe range from 2 up to 20 μs at 77 K irrespective of doping $< 10^{15} \text{ cm}^{-3}$. The MWIR carrier lifetime are substantially longer assuming 2 up to 60 μs . However, several papers published in the last decade have shown τ_{SRH} significantly higher in low temperature range and low doping concentrations, above 200 μs up to even 50 ms versus cut-off wavelength [20] see Table 1. The range of low doping that can be reproducibly obtained in Teledyne Technologies HgCdTe epilayers grown by MBE is $\sim 10^{13} \text{ cm}^{-3}$. Gravrand et al. [24] published that for most tested MWIR photodiodes from CEA Leti and Lynred by Sofradir & Ulis, the estimated SRH carrier lifetimes [from direct measurements (photoconductive or photoluminescence decay) and indirect estimates from current-voltage (I-V) characteristics], are in the range between 10 and 100 μs . Those values are lower than the earlier assessed by US research groups [25]. However, they were estimated for devices with higher doping level in absorber $> 10^{14} \text{ cm}^{-3}$. However, from just published announcement results, Teledyne Technologies confirmed fabrication of depletion layer limited P-i-N HgCdTe photodiodes with SRH recombination centers exhibiting carrier lifetimes in the range 0.5–10 ms [25].

Table 1. Summary of the SRH carrier lifetimes determined based on current-voltage characteristics (data after reference [20]).

Spectral Range	x Composition	SRH Lifetime (μs)	Temperature (K)
SWIR	0.455	>3000	180
MWIR	0.30	>1000	110
MWIR	0.30	$\sim 50,000$	89
LWIR	0.225	>100	60

All SRH lifetimes estimated for HgCdTe are usually carried out for temperatures below 300 K. Their extrapolation to 300 K to predict the photodiode operation behavior is questionable. In our estimates we assume $\tau_{SRH} = 1 \text{ ms}$, which is supported by experimental data reached by Leonardo DRS and Teledyne Technologies research groups.

Figure 2a shows a schematic P-i-N detector energy band profile for a reverse voltage. The active region consists of an undoped i-layer (often called as ν region exhibiting low n-doping) sandwiched between wider bandgap cap (P) and buffer (N) region (see Figure 2b) [26]. Very low doping in the absorber ($< 5 \times 10^{13} \text{ cm}^{-3}$) is required to allow full depletion at zero or low reverse voltage. The surrounded wide gap contact layers are designed to reduce the dark current generation from these regions and to prevent tunneling current under reverse bias. Moreover, fully depleted absorber surrounded by wide bandgap regions theoretically reduces 1/f and burst noise. As previously mentioned,

the fully depleted P-i-N architecture is compatible with the small pixel size, meeting the requirements of low crosstalk thanks to the built-in electric field [20,26].

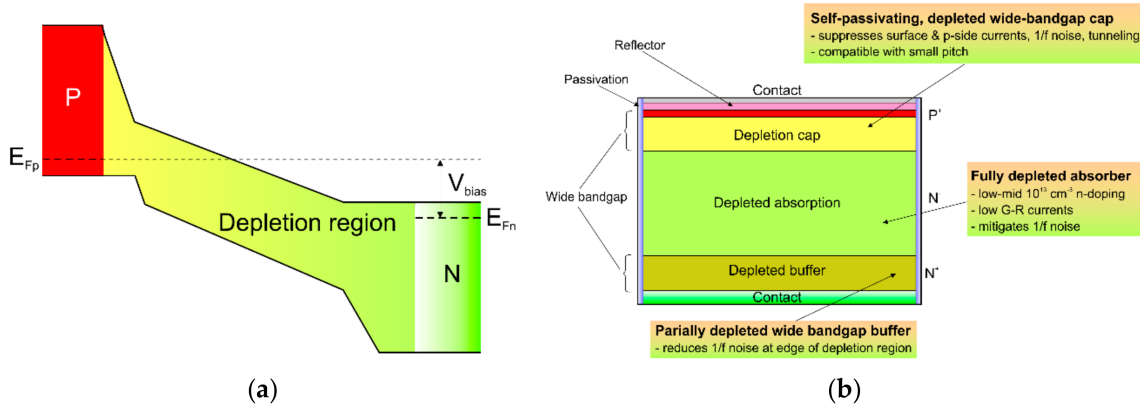


Figure 2. P-i-N detector: (a) energy band profile under reverse bias, (b) heterojunction architecture (adapted after reference [26]).

In P-i-N design, the choice of absorber thickness should be a trade-off between the response time and QE (or responsivity). To reach short response times, the absorber thickness should be thin and fully depleted. For high QE the absorption region should be thick enough to effectively collect photogenerated carriers. However, to enhance QE while maintaining high response time, an external resonant microcavity was demonstrated [8]. In this design, absorber is placed inside a cavity so that more photons can be absorbed even in low detection volume.

3.2. Dark Current Density

In general, for the fully depleted P-i-N photodiode, the current is built by diffusion from N and P regions (that depends on SRH and Auger generations) and depletion current only determined by SRH generation in the space charge region. Influence of radiative recombination is still debatable but is not considered as a limiting factor of the small pixel HgCdTe photodiodes. Moreover, due to the photon recycling effect, the radiative recombination contribution can be significantly reduced [27]. By that reason in our discussion the radiative recombination is omitted.

The diffusion current of P-i-N HgCdTe photodiode structure arises from the thermal generation of carriers in thick, non-depleted absorber and is dependent on the Auger and SRH generation in n-type semiconductor [20]

$$J_{dif} = \frac{qn_i^2 t_{dif}}{n} \left(\frac{1}{\tau_{A1}} + \frac{1}{\tau_{SRH}} \right), \quad (4)$$

where q —Electron charge, n_i —Intrinsic carrier concentration, n —Electron concentration, t_{dif} —Diffusion region thickness, τ_{A1} —Auger 1 lifetime, and τ_{SRH} —SRH lifetime. Auger 1 lifetime relates to the hole, electron, and intrinsic carrier concentrations, and τ_{A1} is given by equation

$$\tau_{A1} = \frac{2\tau_{A1}^i n_i^2}{n(n+p)}, \quad (5)$$

where p —Hole concentration and τ_{A1} —Intrinsic Auger 1 lifetime. For a low temperature operation or a non-equilibrium active volume, when the majority carrier concentration is held equal to the majority carrier doping level [and intrinsically generated majority carriers are excluded ($p \ll n \approx N_{dop}$)], Equation (5) becomes

$$\tau_{A1} = \frac{2\tau_{A1}^i n_i^2}{n^2}. \quad (6)$$

The shortest SRH lifetime occurs through centers located approximately at the intrinsic energy level in the semiconductor bandgap. Then, for the field-free region in an n volume ($n \gg p$), τ_{SRH} is given by

$$\tau_{SRH} = \frac{\tau_{no}n_i + \tau_{po}(n + n_i)}{n}, \quad (7)$$

where τ_{no} and τ_{po} —specific SRH lifetimes. At low temperatures, where $n > n_i$, we have $\tau_{SRH} \approx \tau_{po}$. At high temperatures where $n \approx n_i$, we have $\tau_{SRH} \approx \tau_{no} + \tau_{po}$. For a non-equilibrium active volume, $\tau_{SRH} \approx (\tau_{no} + \tau_{po})n_i/n$ exhibits a temperature dependence given by n_i .

The second component is the depletion current arising from the portion of the absorber that becomes depleted. The depletion current density can be assessed by the relation

$$J_{dep} = \frac{qn_i t_{dep}}{\tau_{no} + \tau_{po}}, \quad (8)$$

where t_{dep} —Depletion region thickness.

The P-i-N HOT detector is characterized by useful properties at reverse voltage. Figure 3 shows the calculated reverse voltage required to completely deplete a 5-μm-thick absorber for selected doping level. For the Rule 7 with doping range about 10^{15} cm^{-3} , a 5-μm-thick absorber can be fully depleted by applying a relatively high reverse bias between 10 V and 30 V. On the other hand, for the doping level reached presently at Teledyne Technologies ($\sim 10^{13} \text{ cm}^{-3}$), the 5-μm-thick active layer can be fully depleted for reverse bias from zero up to 0.4 V.

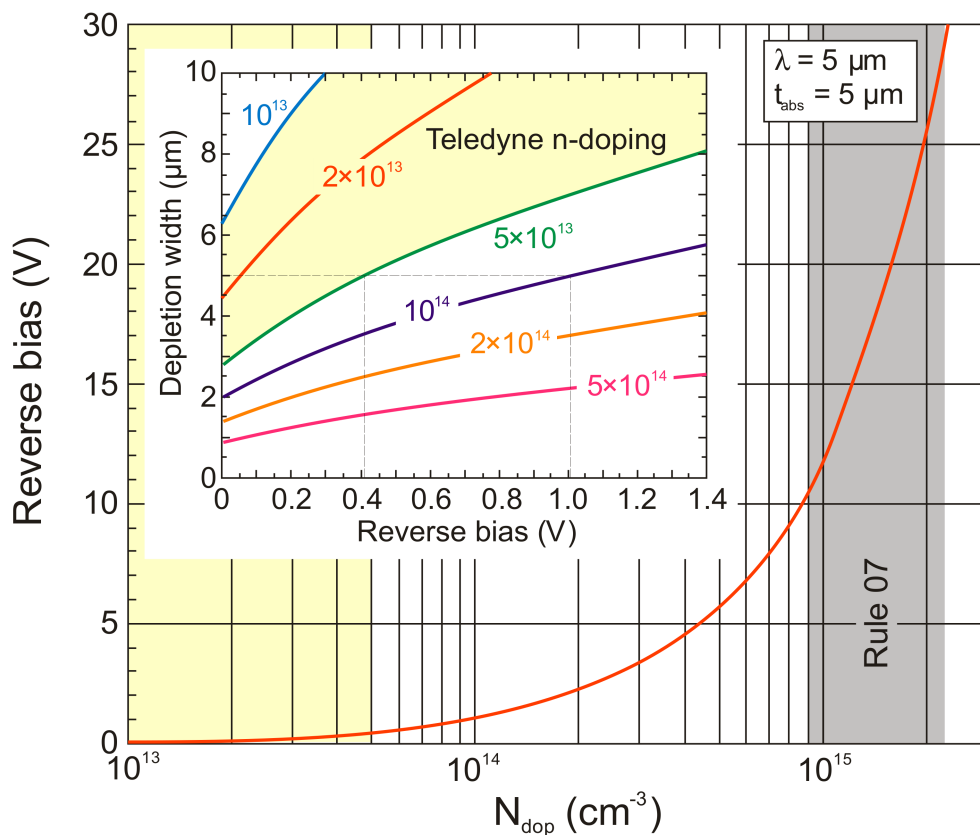


Figure 3. Calculated reverse voltage versus doping concentration required to deplete a 5-μm-thick MWIR HgCdTe absorber. Inset: absorber depletion thickness versus reverse bias and selected doping concentration.

If P-i-N photodiode operates under reverse bias, Auger suppression effect should be considered. This effect is important in HOT condition when $n_i \gg N_{dop}$. In non-

equilibrium, large number of intrinsic carriers can be swept-out of the absorber region. It is expected that this impact is larger for lower n-type doping levels since n_i is proportionately higher. At very low level of n-type doping (about 10^{13} cm^{-3}) the P-i-N photodiode ultimate performance is influenced by SRH recombination and neither Auger recombination nor Auger suppression.

As is shown in Figure 4, for the sufficiently long SRH carrier lifetime in HgCdTe, the internal photodiode current is limited, and the performance is contributed by the background radiation. Its influence is shown for four background temperatures: 300, 200, 100 and 50 K. Lee et al. suggested to replace Rule 07 by Law 19 corresponding exactly to the background limited curve for room temperature [25]. The internal photodiode current may be several orders of magnitude below Rule 07 versus given cut-off wavelength and operating temperature. It can be also seen that Rule 07 coincides well with theoretically predicted curve for the Auger-suppressed p-on-n photodiode with absorber doping concentration $N_d = 10^{15} \text{ cm}^{-3}$.

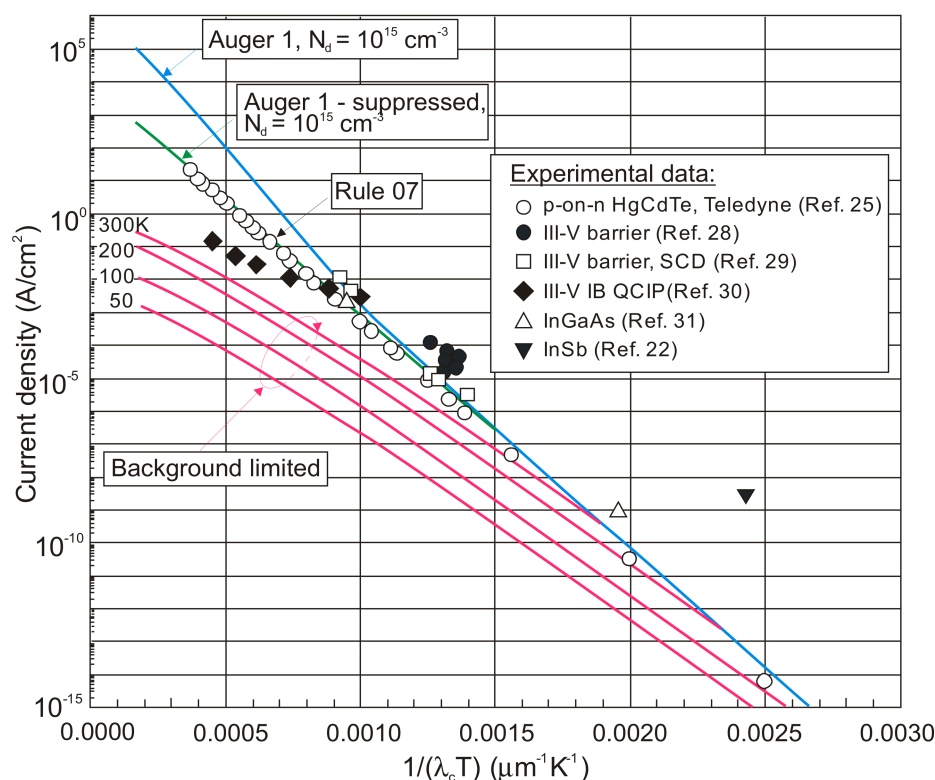


Figure 4. Current density of p-on-n HgCdTe photodiodes versus $1/(\lambda_c T)$ product (adapted after reference [25]). Experimental data is gathered for Teledyne Technologies and alternative technologies [22,25,28–31].

The experimental data for p-on-n HgCdTe photodiodes (Teledyne Technologies) [25] and for III-V barrier detectors (Raytheon Technologies [28] and SCD Semiconductor Devices [29]) operating at about 80 K, and 300 K IB QCIP [30] are presented in Figure 4. It is easy to notice that experimental data for III-V barrier detectors are slightly worse than the p-on-n HgCdTe photodiodes, but III-V IB QCIPs operating at 300 K are even better in LWIR. Figure 4 shows also representative data for both InSb ($\lambda_c = 5.3 \mu\text{m}$, $T = 78 \text{ K}$) and InGaAs ($\lambda_c = 1.7$ and $3.6 \mu\text{m}$, $T = 300 \text{ K}$) photodiodes. InSb detector is characterized by several orders higher dark current density than HgCdTe one, however for optimal InGaAs detectors the dark current density is close to HgCdTe data [31].

The theoretical simulations presented in Figure 4 indicate that the background limited performance (BLIP) has the most impact on detector's current density for small $1/(\lambda_c T)$ products; in other words for photodiodes operating in LWIR and HOT conditions. HgCdTe

photodiodes operating at low temperature become generation-recombination limited due to the SRH centers influence the lifetime in the millisecond range.

Figure 5 shows the current density calculated using Rule 07 (determined for diffusion limited P-on-n photodiodes) and Law 19 (which exactly equals to the background radiation current density) versus temperature for short-wave infrared (SWIR: $\lambda_c = 3 \mu\text{m}$), MWIR (5 μm), and LWIR (10 μm) absorber.

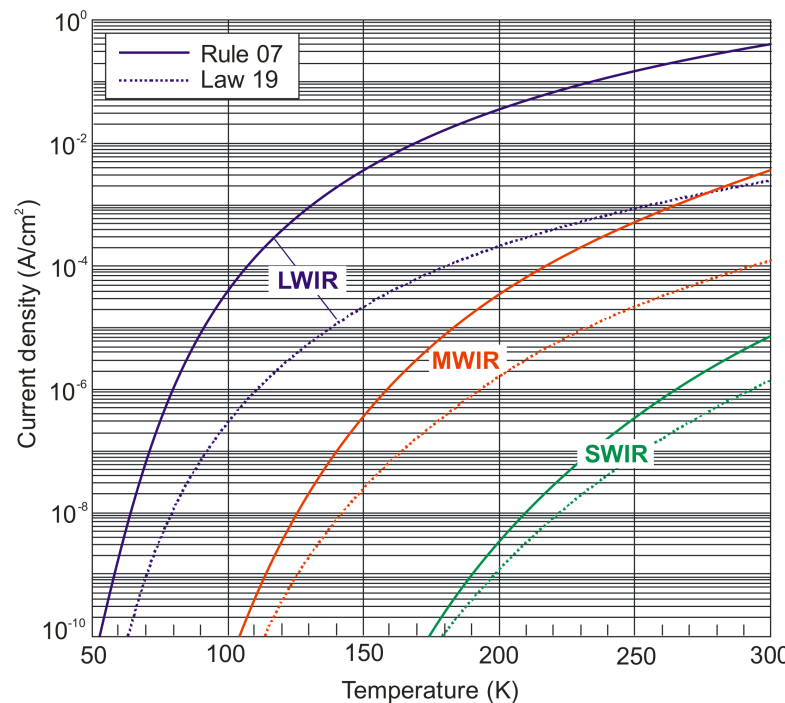


Figure 5. Calculated current density versus temperature using Law 19 and Rule 07 for SWIR ($\lambda_c = 3 \mu\text{m}$), MWIR ($\lambda_c = 5 \mu\text{m}$), and LWIR ($\lambda_c = 10 \mu\text{m}$) HgCdTe absorber.

If the fully depleted P-i-N detector is influenced by the background current, a certain minimal value of SRH lifetime is required. The SRH lifetime calculations were made under condition where depletion dark current equals the background radiation current

$$J_{dep} = J_{BLIP}. \quad (9)$$

It was assumed that the 5- μm thick absorber is fully depleted.

The SRH lifetime at which the fully depleted P-i-N photodiode reaches the BLIP limit is presented in Figure 6. As shown, the SRH lifetime required to reach BLIP limit decreases versus temperature (nevertheless fully depleted P-i-N photodiodes are particularly interesting in HOT conditions). What more, for LWIR detectors, it is possible to reach BLIP for shorter carrier lifetimes. At 300 K and 5- μm fully depleted thick absorber, these carrier lifetimes are 15 ms for SWIR, 150 μs for MWIR and 28 μs for LWIR, respectively.

The Teledyne Technologies experimentally measured SRH lifetimes for 10- μm cut-off HgCdTe are higher than 100 ms (extracted at 30 K) [26]. Despite the fact that at 300 K the carrier lifetimes are likely to be at least 10 times lower (what results from a high thermal velocity increasing the carrier capture probability by the recombination centre), those low SRH lifetimes enable to reach BLIP limit. This prediction is supported by theoretical simulation presented in reference [32].

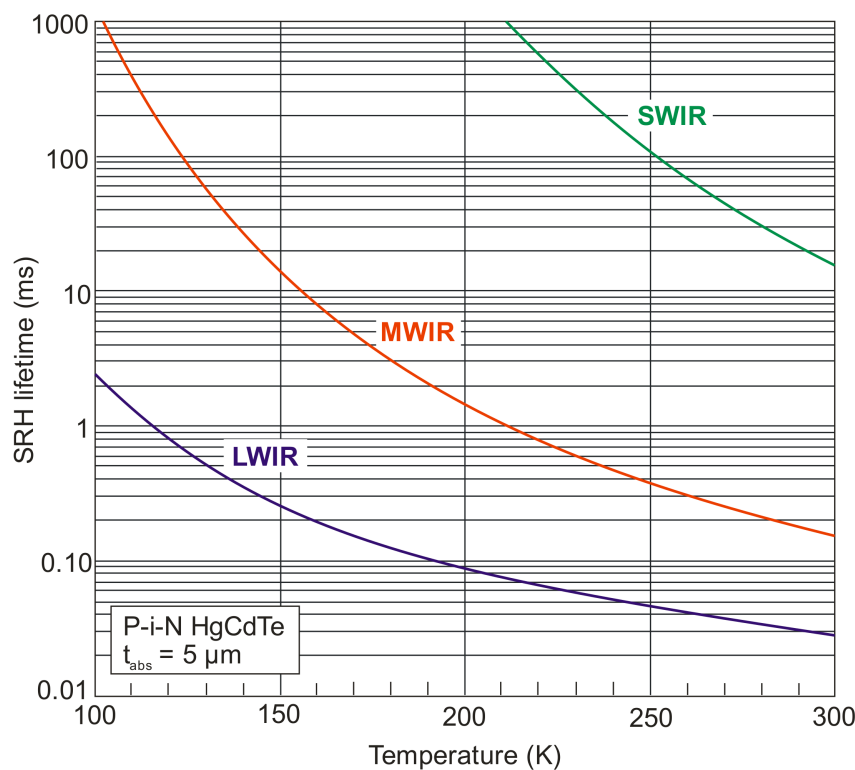


Figure 6. The SRH lifetime versus temperature where fully depleted P-i-N HgCdTe detector depletion dark current equals the background radiation current. The calculations were carried out for SWIR (3 μm), MWIR (5 μm), and LWIR (10 μm) absorbers.

3.3. Detectivity

The detector's detectivity, D^* is related to the current responsivity, R_i [see Equation (13)] and noise current, i_n , and can be given by relation

$$D^* = \frac{R_i}{i_n}. \quad (10)$$

For the non-equilibrium devices, the i_n value can be calculated assuming thermal Johnson-Nyquist and shot noises contribution by the following expression

$$i_n = \sqrt{\frac{4k_B T}{R_0 A} + 2q J_{dark}}, \quad (11)$$

where k_B —Boltzmann constant, $R_0 A$ —Dynamic resistance area product and J_{dark} —dark current density.

The performance of P-i-N MWIR HgCdTe photodiode ($\lambda_c = 5 \mu\text{m}$) is presented in Figure 7.

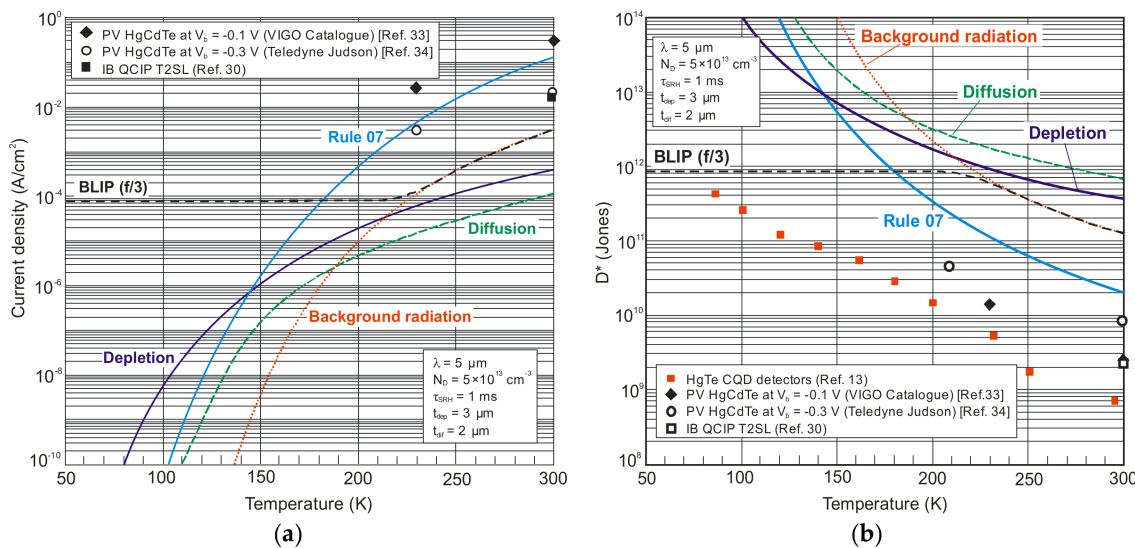


Figure 7. MWIR P-i-N HgCdTe photodiode performance with $\tau_{SRH} = 1 ms$ and absorber doping $5 \times 10^{13} cm^{-3}$: (a) diffusion and depletion current components versus temperature, (b) detectivity versus temperature. The thickness of active region: $t = 5 \mu m$ and consists of $t_{dif} = 2 \mu m$ and $t_{dep} = 3 \mu m$. The experimental data is taken from different sources as marked. PV—Photodiode, CQD—Colloidal quantum dot, IB QCIP—Interband quantum cascade infrared photodetector. Experimental data is taken from [30,33,34].

As is shown in Figure 7a, the Teledyne Judson experimentally measured current densities, at the bias $-0.3 V$, are close to BLIP (f/3) curve and they are located less than one order of magnitude above this limit [34]. The current density at 300 K is even lower than predicted by Rule 07. The measured current densities presented by VIGO System are close to one order of magnitude higher, however in this case they were measured at lower reverse bias, $-0.1 V$, with less effective Auger suppression [33]. It is interesting to notice, that the performance of IB QCIP based on T2SLs InAs/GaSb coincides well with upper experimental data for HgCdTe photodiodes at 300 K [30].

Figure 7a shows the diffusion and depletion dark current components versus temperature assuming $1 ms$ SRH carrier lifetime, $5 \mu m$ thick absorber and doping $5 \times 10^{13} cm^{-3}$. The diffusion component associated with Auger 1 mechanism is eliminated because of the absence of majority carriers due to exclusion and extraction effects [35,36]. The background radiation calculated assuming f/3 optics has decisive influence on dark current. It should be mentioned here that the background flux current is determined by the net flux through the optics (limited by f/#) plus the flux from the cold shield. This effect is shown by increased BLIP (f/3) influence on dark current at temperature $>220 K$.

Figure 7b shows calculated detectivity versus temperature for MWIR P-i-N HgCdTe photodiode assuming identical parameters as taken in calculations presented in Figure 7a ($\lambda_c = 5 \mu m$, $\tau_{SRH} = 1 ms$, $t = 5 \mu m$, $N_{dop} = 5 \times 10^{13} cm^{-3}$). The current responsivity was estimated assuming QE = 1 (however typical QE reaches reasonable value ~ 0.7). As is shown, for MWIR photodiode with 5- μm cut-off wavelength and low doping in active region, detectivity, D^* is limited by background and is about one order of magnitude higher than predicted by the Rule 07. The experimental data given for HgCdTe photodiodes in Teledyne Judson and VIGO System catalogues are more than one order of magnitude below background flux limitation for the f/3 optics.

4. Interband Quantum Cascade Infrared Photodetectors (IB QCIPs)

A low diffusion length, weak absorption and finally low dynamic resistance limit the performance of conventional p-n LWIR HgCdTe HOT detectors with doping concentrations in absorbers $> 10^{16} cm^{-3}$. The QE is limited since the absorption depth of LWIR ($\lambda > 5 \mu m$) is much longer than the diffusion length allowing charge carriers photogenerated at distance shorter than the diffusion length to be collected by the contacts. For example, estimates

show that for 10.6- μm detector the absorption depth is $\sim 12 \mu\text{m}$ while the ambipolar diffusion length is less than $2 \mu\text{m}$. In consequence, the QE is reduced to $\sim 15\%$ [9].

To overcome above problems, the multiple heterojunction devices based on thin elements connected in series were proposed, where a proper example is a detector with junctions perpendicular to the substrate, introduced in 1995. The multi-heterojunction device shown in Figure 8a contains backside illuminated n⁺-p-P detectors connected in series. The advantages of such design are a high voltage responsivity, a short response time while on the other hand the response depends on polarization of incident radiation and is nonuniform across the active area.

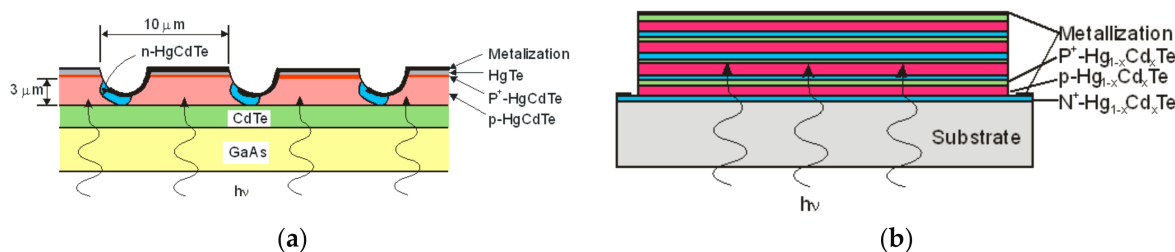


Figure 8. Backside illuminated multiple HgCdTe heterojunction devices: (a) junction's planes perpendicular to the surface, and (b) 4-cells stacked multiple detector (after reference [8]).

More promising design is the stacked tunnel junctions connected in series as shown in Figure 8b being similar to multi-junction solar cells. Potentially, this device can reach both good QE, high differential resistance, and fast response. As presented, each cell consists of lightly p-type doped absorber and N⁺/P⁺ wide-bandgap highly doped contact layers. The heterojunction contacts collect the photogenerated carriers absorbed in every active layer. However, practical problem is related to the resistance of the adjacent N⁺ and P⁺ layers.

In the last decade, several designs of the multi-stage IR devices have been developed. They are based on III-V semiconductors and might be now divided into two classes: mentioned earlier interband (IB) ambipolar QCIPs and intersubband (IS) unipolar QCIPs. The first study on IS QCIPs began about two decades ago [11] as the photodetectors were developed from the quantum cascade lasers (QCLs). However, currently IB QCIPs show the higher performance in comparison with IS QCIPs due to the relatively much longer carrier lifetime. The IB QCIPs saturation current density is reported to be almost two orders of magnitude lower than for IS QCIPs [30].

Schematic illustration of IB QCIP is presented in Figure 9 where every single active layer is sandwiched between the relaxation and tunneling layers forming a cascade stage. The thickness of the single active layer should be thinner than the diffusion length to effectively collect all photogenerated carriers. The diffusion length restriction in traditional thick absorber detectors is bypassed by using the discrete absorber design imposing recombination of the photogenerated carriers in the next stage within short transport distance. The single thin absorbers are connected in series and the total thickness of the active layer can be even thicker than the absorption depth. The photocurrent is determined by carriers generated in the single absorber (one stage) and is independent of the number of stages meaning that the photons absorbed in following stages do not increase the net photocurrent but only provide the current continuity through the device. The noise suppression for shorter individual absorbers is the advantage of QCIP design. The QCIP detectivity, D^{*} is influenced by the Johnson and shot noises that is proportional to \sqrt{N} according to the relation [37]

$$i_n = \sqrt{\frac{4k_B T}{NR_0 A} + \frac{2qJ_{dark}}{N}}, \quad (12)$$

where N —Number of periods and both dynamic resistance, dark current correspond to one QCIP's period. The optimal number of periods is related to the thickness of the single

absorber, d , and the absorption coefficient and could be expressed as $N = (2\alpha d)^{-1}$ in the first order approximation.

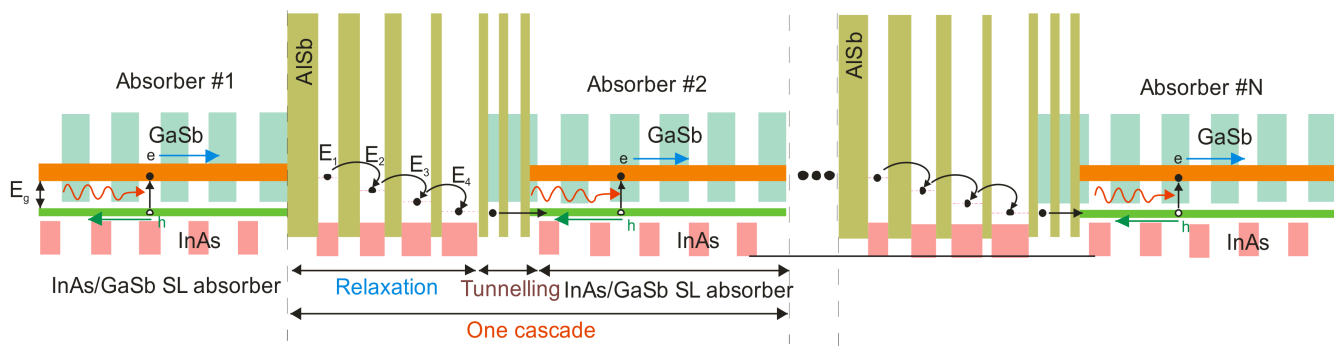


Figure 9. IB QCIP based on T2SL InAs/GaSb active, GaSb/AlSb tunneling and InAs/AlSb relaxation layers (after reference [38]).

The IB QCIPs (with T2SLs absorbers) MBE growth process is challenging where many interfaces and strained thin layers are deposited in structures. Nevertheless, the significant progress has been reached for T2SL based detectors particularly for the LWIR and HOT conditions. They exhibit the capabilities of the IB optical transitions with the exceptional carrier transport properties of the QCIP architectures.

Currently, IB QCIPs has two types of configuration: current-matched (designed to have an equal photocurrent in every single stage) and non-current-matched [39]. Hinkey and Yang described the IB QCIP structure with equal absorbers offering the potential for significant responsivity improvement assuming $\alpha L \leq 0.2$ (αL —Product of the absorption coefficient and the diffusion length) [40]. From a technological point of view, the non-current-matched IB QCIPs (identical absorber thickness in all stages) are simpler to design and grow in comparison to the current-matched ones. The disadvantage of non-current-matched structure is the limited responsivity due to the significant light suppression along the detector's structure. The high electrical gain, lately observed at HOT conditions in these structures, could at least partially compensate in terms of responsivity reduction [41,42].

Despite the development of other technologies, HgCdTe is still the most broadly used adjustable gap semiconductor for IR detectors, to include uncooled operation, and stands as a reference for alternative technologies. Figure 10 demonstrates that T2SL InAs/GaSb IB QCIPs bipolar devices (dashed lines) are proper candidate for HOT conditions. The assessed Johnson-noise limited detectivities under unbiased conditions for IB QCIPs with T2SL InAs/GaSb absorbers (based on the measured R_0A product and responsivity) are comparable with commercially available HgCdTe devices. The performance of both types of detectors is comparable only in SWIR range and IB QCIPs outperform uncooled HgCdTe detectors with a similar LWIR cut-off wavelength. Another advantage of IB QCIPs is related to the III-V semiconductors strong covalent bonding allowing for operation at temperatures close to 400 °C being not possible for HgCdTe.

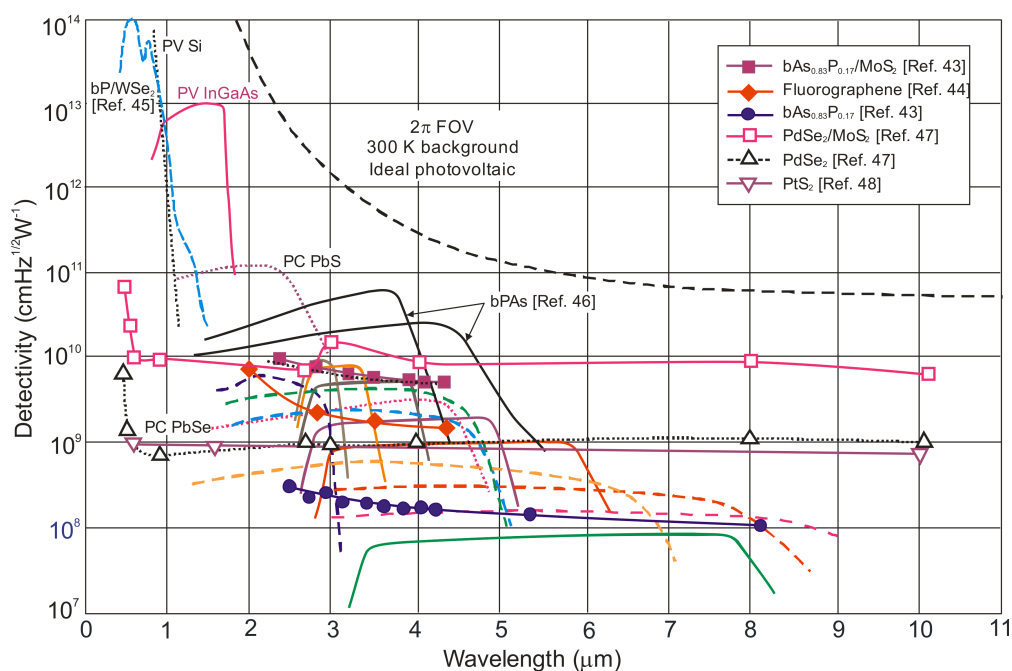


Figure 10. Room-temperature spectral detectivity curves of the commercially available photodetectors [PV Si and InGaAs, PC PbS and PbSe, HgCdTe photodiodes (solid lines reference [33])]. The spectral detectivity curves of new emerging T2SL IB QCIPs are marked by dashed lines (reference 38). Also the experimental data for different types of 2D material photodetectors are included. Experimental data is taken from [43–48]. PC—Photoconductor, PV—Photodiode.

In Figure 10, the representative experimental data for 2D material single photodetectors operating in IR spectral range are also marked. It can be seen that in MWIR the performance of black phosphorous-arsenic (bPAs) photodetectors outperforms commercially available uncooled HgCdTe photodiodes, while in LWIR, the detectivity, D^* of the transition metal dichalcogenide (TMD) photodetectors (PdSe₂/MoS₂ heterostructure) is the best. More detailed comments about these results are included in Section 5.2.

Figure 11 compares the peak detectivity, D^* for HgCdTe photodiodes [33] and InAs/GaSb T2SIs IB QCIPs [38] operating at 300 K with bPAs and TMD photodetectors. In MWIR the performance of bPAs devices is higher than commercially available uncooled HgCdTe photodiodes, while in LWIR, the detectivity, D^* of the TMD photodetectors is the best. The HgCdTe and IB QCIPs response time at 300 K, typically in the order of nanoseconds, is significantly shorter than for 2D material photodetectors.

Figure 12 gathers the highest detectivity, D^* values published in literature for different types of single element photodetectors operating at room temperature. This fact should be clearly emphasized since detectivity, D^* data marked for commercial photodetectors is typical for pixels of IR FPAs. Figure 12 also presents the fundamental indicator for future trend in development of HOT IR photodetectors. At present stage of HgCdTe technology, the semiempirical Rule 07 is found not to fulfil primary expectations. It is shown that the detectivity, D^* of low-doping P-i-N HgCdTe ($5 \times 10^{13} \text{ cm}^{-3}$) photodiodes, operating at 300 K in spectral band above 3 μm , is limited by background radiation (with detectivity, D^* level above 10^{10} Jones, not limited by detector itself) and can be improved more than one order of magnitude in comparison with predicted by Rule 07. Between different material systems used in fabrication of HOT LWIR photodetectors, only HgCdTe can fulfill required expectations: low doping concentration— 10^{13} cm^{-3} and high SRH carrier lifetime above 1 ms. In this context, 2D material photodetectors and CQD photodetectors cannot compete with HgCdTe photodiodes. The above assessments provide further inspiration for reaching low-cost and high performance MWIR and LWIR HgCdTe FPAs operating in HOT conditions. The performance of T2SL IB QCIPs is close to HgCdTe photodiodes

and quantum cascade photodetectors can operate in temperature > 300 K; however, their disadvantage is a challenging technology and higher fabrication cost.

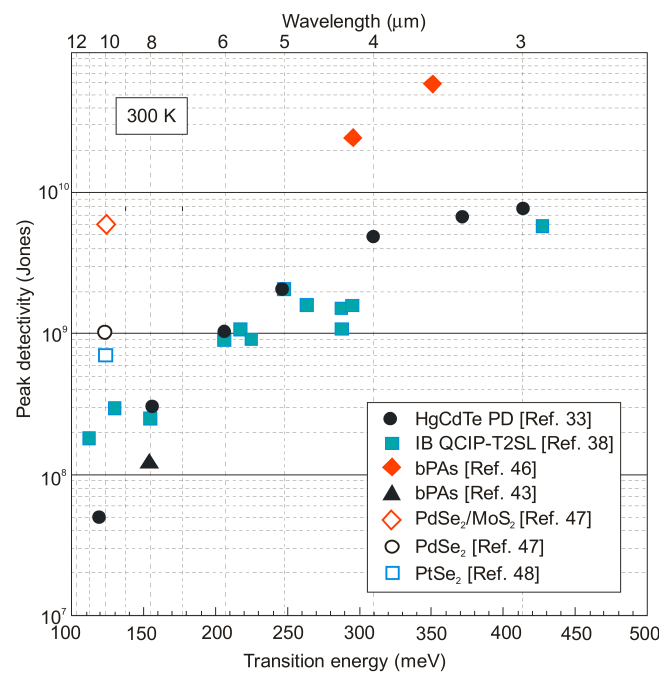


Figure 11. HgCdTe photodiodes, T2SLs InAs/GaSb IB QCIPs and representative 2D material photodetectors peak detectivity, D^* comparison for 300 K. The measured data for HgCdTe photodiodes according to the VIGO System catalogue [33]. Data for IB QCIPs extracted from selected papers [38]. Data for selected 2D materials is taken from [33,38,43,46–48].

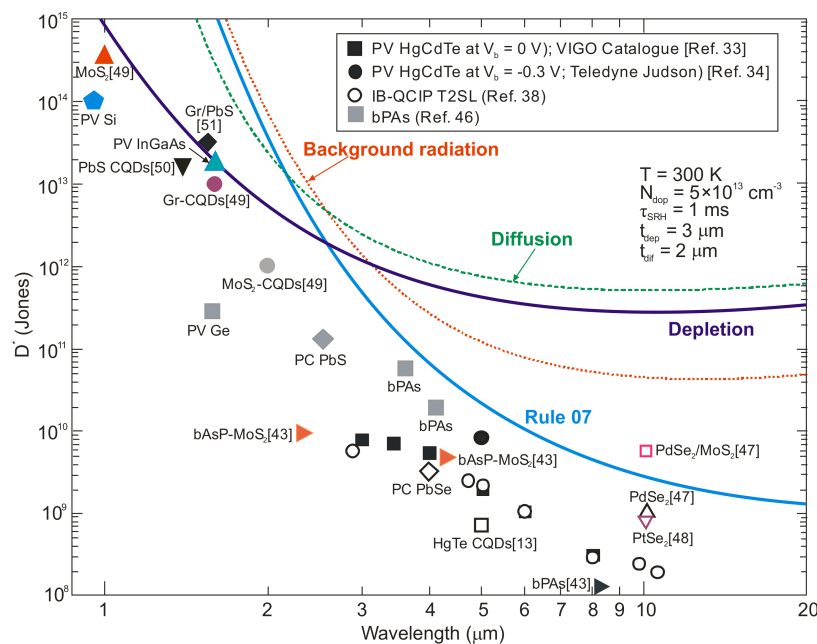


Figure 12. Detectivity, D^* versus wavelength for the commercially available room-temperature IR photodetectors (PV Si and Ge, PV InGaAs, PC PbS and PbSe, PV HgCdTe). There is also included experimental data for IB QCIP T2SLs, different type of 2D material and CQD photodetectors taken from literature as marked. The theoretical curves are calculated for the P-i-N HOT HgCdTe devices assuming $\tau_{\text{SRH}} = 1$ ms, the absorber doping $5 \times 10^{13} \text{ cm}^{-3}$ and the active region thickness $t = 5 \mu\text{m}$. Experimental data is taken from [13,33,34,38,43,46–51]. PC—Photoconductor, PV—Photodiode.

5. 2D Material Infrared Photodetectors

Graphene and other two-dimensional (2D) materials, due to uncommon electronic and optical properties, are considered to be promising candidates for IR photodetectors [52]. The further development of graphene-based photodetectors is a consequence of the high dark current the gapless material significantly limits the sensitivity. The discovery of new 2D materials with direct energy gaps in a wide spectral range (from the visible to the IR) has set a new direction for detector's design and fabrication. Although the technology readiness, the 2D materials are still at low level of development, the detectors' manufacturability and reproducibility have been challenging (this topic is widely studied in research laboratories around the globe).

Nicolosi et al. [53] distinguished the different types of 2D materials and refined them into different families (see Figure 13) covering a broad range of electrical and optical properties:

- transition metal dichalcogenides (TMDs),
- black phosphorus (bP), metal halides (e.g., PbI₂, MgBr₂), metal oxides (such as MnO₂ and MnO₃), double hydroxides, III-Vs (such as InSe and GaS), V-VIs (such as Bi₂Te₃ and Sb₂Se₃), and
- atomically thin hexagonal boron nitride (h-BN, similar to hexagonal sheets of graphene),
- halide perovskites.

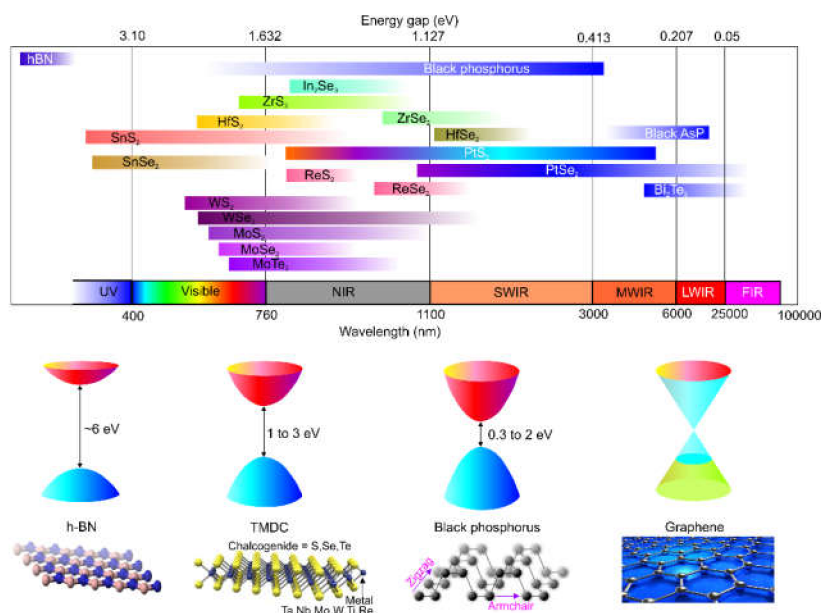


Figure 13. Energy bandgap of the selected layered semiconductors versus wavelength. The energy bandgap exhibits the dependence on the layers number, strain level and chemical doping. FIR—Far infrared; LWIR—Long wavelength infrared; MWIR—Mid wavelength infrared; SWIR—Short wavelength infrared; NIR—Near infrared; UV—Ultraviolet.

2D materials have their roots in layered van der Waals (vdW) solids. Atomic layers are built by in-plane atoms connected by ionic or tight covalent bonds along 2D directions. Each layer is bonded with another by a weak vdW interactions along out-of-plane direction. Such design causes that many of 2D materials could be mechanically exfoliated from bulk single crystals. What more, due to a weak bond between layers, a mixing of different 2D materials together is also possible with the flexibility of the heterostructures.

Energy band profiles of the layered materials differ from their bulk counterparts. Since the material gets thinner from the bulk to the monolayer, e.g., for TMDs the band structure transits from smaller indirect transition to a larger direct due to quantum confinement effects, thus, the bandgap (operating wavelength) can be adjusted by the layers number. Moreover, large strains occurring in these materials strongly affect their optical

and electronic properties. A high absorption coefficient of TMDs (typically 10^4 – 10^6 cm $^{-1}$) results from dipole transitions between localized d-states and excitonic coupling of such transitions. Thanks to that, >95% of the sunlight is absorbed in sub-micrometer thickness TMD films, while carrier mobility is low (typically less than 250 cm 2 /Vs). Despite the fact that the mobility can be improved by increasing the number of TMDs layers, this disadvantage is difficult to circumvent. The carrier density depends on the doping levels and the number of recombination centers, and typically reaches 10^{12} cm $^{-2}$ [54].

In comparison to graphene, TMDs, like molybdenum disulfide (MoS₂), tungsten disulfide (WS₂) and molybdenum diselenide (MoSe₂) is characterized by higher absorption in the visible and NIR ranges. As presented in Figure 13, the 2D bandgap profile is so different what allows to cover a very broad range from the UV to IR. For current status of technology, only graphene-based, black phosphorus-arsenic (bPAs), noble metal dichalcogenides, and bismuthene (like Bi₂Te₃ and Bi₂Se₃) are treated as a main player in IR and also THz regions. Since 2D TMDs are limited to UV-NIR, bP can be adjusted to below 0.3 eV by As doping. Due to high mobility, up to 3000 cm 2 /Vs, bP is a proper candidate for high sensitivity and fast speed photodetection. Recently published paper indicates that low bandgap 2D noble metal dichalcogenides could be novel platform for 300 K LWIR detectors [47].

From the practical applications point of view, the most important aspect is the stability of the material determining the reliability and lifetime of the device. This is a main disadvantage of most 2D materials. Due to only one or several-atoms thick of the active detector layer, 2D materials are susceptible to ambient environment (especially bP degrades quickly under 300 K conditions). The role of different ambient species has remained debatable [55]. The layered bP devices are still in development stage with many unsolved issues and ideas [56]. On the contrary, the air-stability properties have been demonstrated for noble metal dichalcogenides [47].

5.1. 2D Material Photodetectors: Current Responsivity Versus Response Time

The detector's current responsivity is given by equation

$$R_i = \frac{\lambda\eta}{hc} qg, \quad (13)$$

and is determined by the QE (η) and photoelectrical gain, g . The QE is given by the number of electron-hole pairs generated per incident photon and shows how the detector is coupled to the impinging radiation. The second parameter, the photoelectrical gain describes the number of carriers reaching contacts per one generated pair and shows how well the generated carriers are used to increase photodetector current responsivity. Other symbols of Equation (13) mean: λ —Wavelength, h —Planck constant, q —Electron charge, and c —Light velocity.

In general, the photoelectrical gain is given by

$$g = \frac{\tau}{t_t}, \quad (14)$$

where τ —Carrier lifetime and t_t —Transit time of electrons between the device electrodes. If the drift length, $L_d = v_d\tau$, is less or greater than the distance between electrodes, l , the photoelectrical gain can be less or greater than unity. The value of $L_d > l$ shows that a one carrier swept out by electrode is replaced directly by an equivalent carrier injected by the opposite contact. In this way, a carrier will circulate until it recombines. For the photodiode, the photoelectric gain usually =1, due to separation of minority carriers by the electrical field of depletion region. However, in a hybrid combination of 2D material photodetectors, the photogeneration and carrier transport occur in a separate regions: one for effective light absorption, and the second - to provide fast charge reticulation. In this way, high gain close to 10^8 electrons per one photon, and significant responsivities for SWIR photodetectors have been demonstrated [51].

The simple architecture of hybrid phototransistor, very popular in the 2D material photodetectors design with the fast transfer channel for carriers, is presented in Figure 14. 2D materials with atomic layer thickness are more vulnerable to local electric fields than conventional bulk materials and the photogating effect can strongly modulate the channel conductivity by external gate voltage, V_g . Improvement in the optical gain is particularly important since the QE is suppressed because of the weak absorption in 2D materials. This effect is especially seen in LWIR region, where the light absorption is weak. In the case of hybrid detector shown in Figure 14a, the holes are injected into transporting channel, whereas the electrons remain in the photoactive layer. The injected charges can reticulate even several thousand times before recombination, giving contribution to the gain under illumination. The photocarrier lifetime is enhanced through both the bandgap profile and defect engineering, and at the same time the trapping mechanisms limit the response time of photodetector even to several seconds. The trade-off between improvement in responsivity and response time must be considered during optimization process.

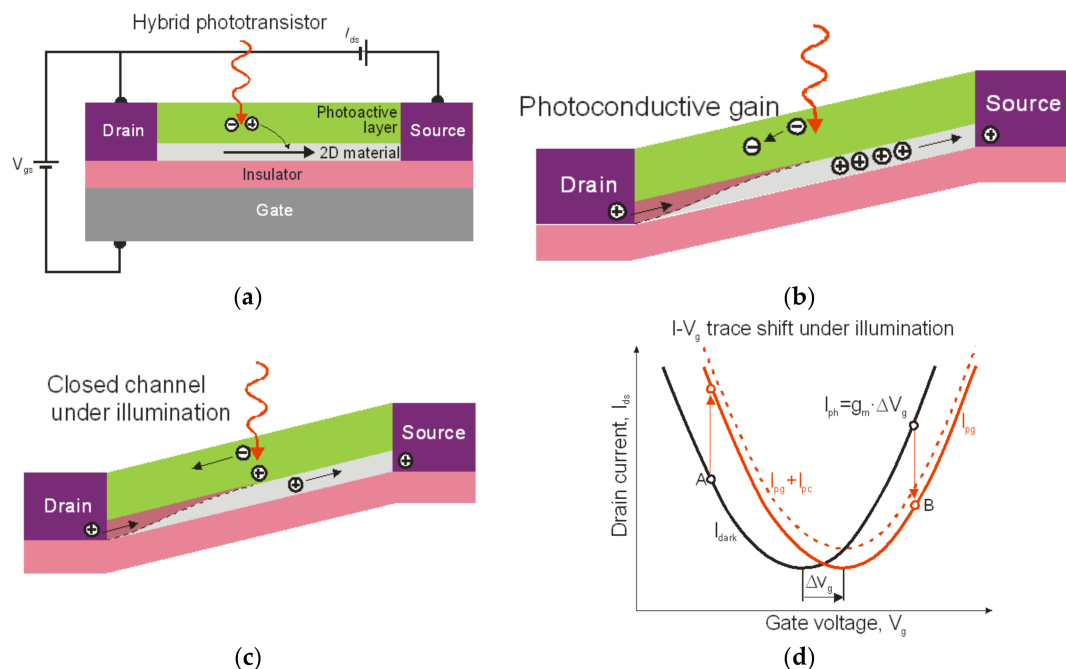


Figure 14. Photogating effect in 2D material photodetectors: (a) the operation of hybrid phototransistor, (b) closed channel under illumination, (c) photoconductive gain, and (d) I-V_g trace under illumination.

The photocurrent versus photogating effect can be given by [57]

$$I_{ph} = g_m \Delta V_g, \quad (15)$$

where g_m —Transconductance, ΔV_g —Equivalent photoinduced bias. Figure 14d indicates a shift of the $I_{ds}(V_g)$ trace after the light illumination. Generally, both positive and negative photoconductance effects are observed in hybrid 2D structures and operating points A and B, related to g_m and ΔV_g , perform opposite directions.

Figure 15 compares the graphene-based detectors responsivity operating in visible and NIR with silicon and InGaAs photodiodes commercially available on the market [58,59]. The highest current responsivity, above 10^7 A/W, has been reached for hybrid Gr/quantum dot (QD) photodetectors with enhancement trapped charge lifetimes. As shown, the graphene high mobility along with the extension of the charges lifetime trapped in QDs caused a photodetector responsivity up to seven orders of magnitude higher in relation to the standard bulk photodiodes, where $g \approx 1$. Higher responsivity of Si avalanche photodiode (APD), up to 100 A/W, is caused by avalanche process. However, due to the

long lifetime of trapped carriers, the response time of 2D material photodetectors is very slow (<10 Hz), what considerably limits real detector functions.

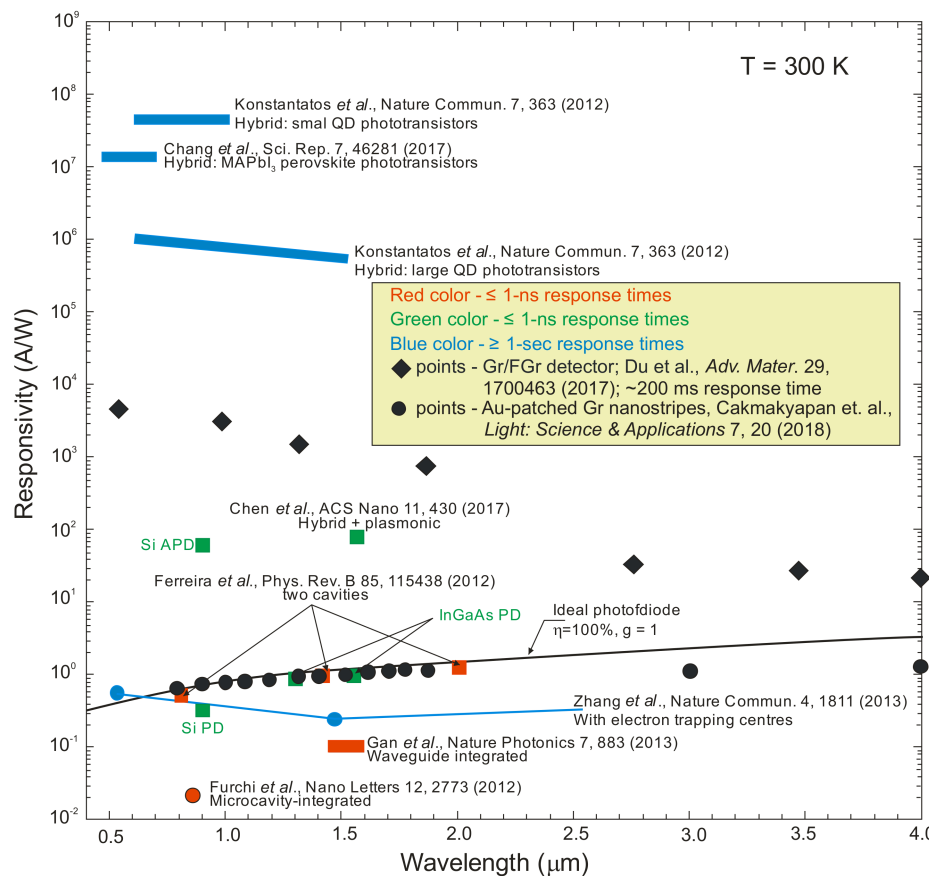


Figure 15. The graphene-based photodetectors spectral responsivity compared with commercial detectors. Black line presents spectral responsivity for ideal photodiode with 100% QE and $g = 1$. Red and green colors correspond to ≤ 1 ns, while the blue color ≥ 1 second response times. The graphene detectors are labelled with proper reference and brief description. The commercial photodiodes are marked in green (adapted after reference [58,59]).

It is interesting to underline the unusual electrical and optical properties of gold patched graphene nanostripe detectors presented by Cakmakyapan et al. [60]. The photodetector exhibits a spectral response in the ultrabroad range from visible to the IR with high responsivity ranging from 0.6 A/W (for wavelength 800 nm) to 11.65 A/W (for 20 μ m) and frequency exceeding 50 GHz. As is shown in Figure 15, its current responsivity (black circles) coincides well with curve (black line) theoretically predicted for ideal photodiode in NIR spectral range.

2D materials show potential for operation in wide spectral range from UV to THz, although majority of them cover visible and SWIR (see Figure 16). Similarly, for graphene photodetectors, both high responsivity and short response time cannot be reached simultaneously in many 2D material-based photodetectors.

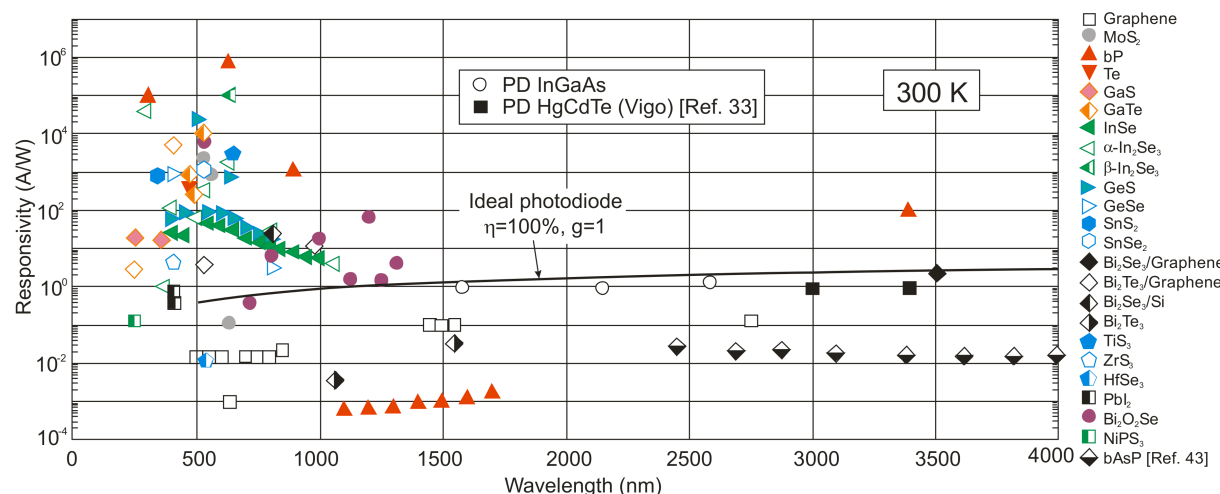


Figure 16. The layered 2D material photodetectors spectral responsivities at 300 K (after reference [43,61]). Black line shows spectral responsivity for ideal photodiode with 100% QE and $g = 1$. The responsivities of commercially available photodetectors (InGaAs and HgCdTe photodiodes) are presented for comparison reasons.

The two major factors determine the development of the 2D material high sensitivity photodetectors. It is a short carrier lifetime and low absorption in a thin active region ($\sim 100\text{--}200$ nm). In consequence, the broadband operation sets a trade-off between high responsivity and response time. The 2D materials-based detectors display a large variation in their responsivity and response time [62–64] about 9 orders of magnitudes as is shown in Figure 17. In order to improve the IR absorption, the multiple layers instead of the single layer are chosen. In photogating effect photodetectors, 2D materials are used as the fast transfer channel for carriers. However, as is mentioned above, their overall disadvantage is the very slow response time attributed to traps and high capacitance. The response time is typically longer than $\sim 1 \times 10^{-2}$ ms, what indicates on considerably longer response time in comparison with commercial silicon, InGaAs, and HgCdTe photodiodes, while for HOT LWIR photodiodes is typically tens of nanoseconds. The up-left blank panel on Figure 17 shows the lack of photodetectors with both high responsivity and short response time. Figure 17 summarizes the responsivity and response time of different 2D material photodetectors. It is shown that black phosphorus is a good candidate for fast detection and falls into a region between graphene and TMDs.

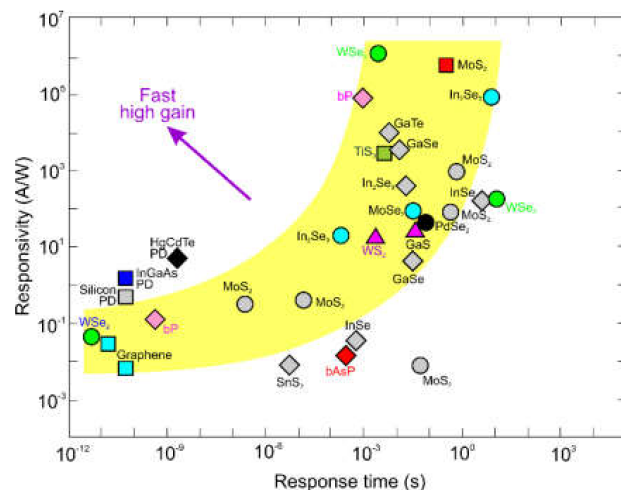


Figure 17. Current responsivity versus response time for HOT 2D material photodetectors in relation to the commercial silicon, InGaAs and HgCdTe detectors (experimental data taken from reference [63]).

5.2. Detectivity: HgCdTe Photodiode Versus 2D Material Photodetectors

Figure 10 presents detectivity, D^* curves gathered from literature for HOT MWIR and LWIR photodetectors both for commercially available devices (PV Si and InGaAs, PC PbS and PbSe, HgCdTe photodiodes) and IB QCIP T2SLs, as well as for 2D material photodetectors. All experimental data gathered in Figure 10 indicates on sub-BLIP photodetectors performance. As is shown, the literature data for 2D material photodetectors in LWIR above $3\text{ }\mu\text{m}$ is limited to several device structures. The Gr/FGr detector utmost detectivity in MWIR is comparable to HgCdTe. However, especially high detectivity (higher than for HgCdTe photodiodes) is demonstrated for black phosphorus arsenic (bPAs) detectors [46]. Their sensitivity enters the second atmospheric transmission window. Here it must be stressed, that the serious drawback of black phosphorus is surface instability in ambient conditions what can considerably limit its prospective applications [55,65]. More promising is stable TMD photodetectors like PdSe₂/MoS₂ heterojunction with record detectivity in LWIR range at room temperature. However, their practical application lies in perfect material synthesis and processing being still under development.

Figure 12 compares the experimental detectivity, D^* published in literature for different types of single element 2D material photodetectors operating at room temperature with theoretically predicted curves for P-i-N HOT HgCdTe detectors. As is presented, the detectivity values for selected 2D material photodetectors are close to data presented for commercial detectors (PV Si and Ge, PV InGaAs, PC PbS and PbSe, PV HgCdTe), and in the case of black phosphorus and TMD detectors are even higher. The enhanced sensitivity of 2D material photodetectors is introduced by bandgap engineering and photogating effect, what degrades the electronic material properties. In consequence, the layered-material photodetectors are characterized by limited linear dynamic range of operation and slow response time.

To summarize the discussion in this section about 2D material IR HOT photodetectors we can conclude that:

- in general, the 2D material IR detectors performance is lower in comparison to the commercially available detectors, especially HgCdTe and new emerging III-V compounds including T2SLs,
- responsivity improvement by using combination of 2D materials with bulks (hybrid photodetectors) owing to the photogating effect causes the limited linear dynamic range due to the charge relaxation time, which lead to decrease in sensitivity with incident optical power,
- responsivity of hybrid and chemically functionalized 2D material photodetectors is comparable with detectors existing on the global market; however, a significant decrease in operating speed (bandwidth) is observed; in general, their response time (millisecond range and longer) is three orders of magnitude longer compared to commercially available photodetectors (microsecond range and shorter) [12],
- the commercialization potential will not just depend on the detector performance, but on the distinct advantages in the ability for fabrication of large scale high quality 2D materials at a low cost,
- experimental data presented by the Teledyne Technologies group [66] support theoretical prediction of background limited P-i-N HgCdTe photodiodes and gives further encouragement for their operation in near room-temperature conditions.

6. Colloidal Quantum Dot Infrared Photodetectors

Research on QD IR photodetectors based on self-assembled epitaxial QDs started in the mid-1990 and were initially very promising. Theoretical estimates carried out by Martyniuk et al. [67] in 2008 indicate that the self-assembled quantum dot infrared photodetectors (QDIPs) are suitable for noncryogenic operation especially in LWIR region. As it happens later, that epitaxial QDs suffer from the size control and low dots density. More recently, an attractive alternative to self-assembled epitaxial QDs has been colloidal

quantum dots (CQDs) with better size tunability of optical features and reduction of fabrication cost.

6.1. Brief View

In the last decade, a significant progress in fabrication of CQD photodetectors has been observed. In this approach, an active region is constructed based on 3D quantum confined nanoparticles synthesized by inorganic chemistry. CQDs offer a promising alternative to the single crystal IR materials (InGaAs, InSb, InAsSb, HgCdTe, as well as T2SLs see Figure 18). These nanoparticles could improve CQD photodetectors performance compared to epitaxial QDs due to many aspects gathered in Table 2 [50,68].

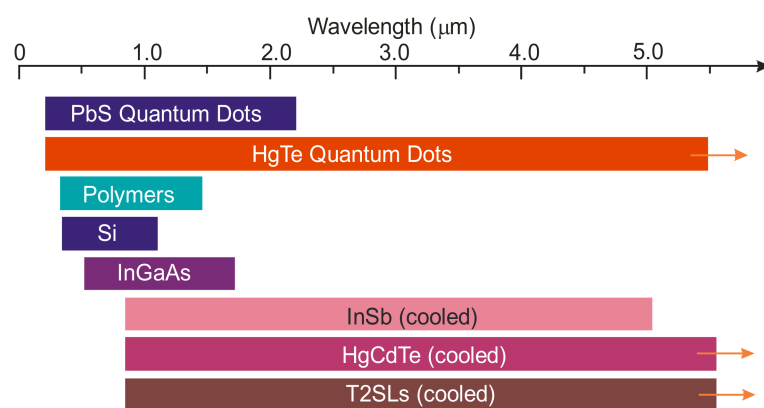


Figure 18. The wavelengths range that can be detected by materials commonly used in imaging applications.

Table 2. CQD photodetectors advantages and disadvantages in comparison with single crystal QD photodetectors.

Advantages	Disadvantages
<ul style="list-style-type: none"> control of dot synthesis and absorption spectrum by ability of QD size-filtering, leading to highly-uniform ensembles much stronger absorption than in Stranski-Krastanov grown QDs due to close-packed of CDs considerable elimination of strains influencing the growth of epitaxial QDs by better selection of absorber materials reduction of cost fabrication (using e.g., such solution as spin coating, inject printing, doctor blade or roll-to-roll printing) compared to epitaxial growth deposition methods are compatible with a variety of flexible substrates and sensing technologies such as CMOS (e.g., direct coating on silicon electronics for imaging) 	<ul style="list-style-type: none"> inferior chemical stability and electronic passivation of the nanomaterials in comparison with epitaxial materials bipolar, interband (or excitonic) transitions across the CQD bandgap (e.g., electrons hopping among QDs and holes transport through the polymer) contrary to the intraband transitions in the epitaxial QDs insulating behaviour due to slow electron transfer through many barrier interfaces in a nanomaterial problems with long term stability due to the large density of interfaces with atoms presenting different or weaker binding high level of 1/f noise due to disordered granular systems

CQD photodetectors are typically fabricated using conducting-polymer/nanocrystal blends, or nanocomposites [13,50,69,70]. Nanocomposites often feature narrow-bandgap, II-VI (HgTe, HgSe) [71,72], PbSe or PbS [73–75]. Usually, the reported IR photodetectors use CQDs embedded in conducting polymer matrices, such as poly [2-methoxy-5-(2-ethylhexyloxy)-1,4-phenylenevinylene] (MEH-PPV).

It is expected that the extension of application of CQD-based devices will be significant, especially in IR imaging which is currently dominated by epitaxial semiconductor and hybrid technologies [76]. Hybrid technology, due to the complexity of production

stages, reduces yield and increases overall cost. The IR CQD-based photodetectors are an alternative solution without these limitations.

The CQD layers are amorphous what permits fabrication of devices directly onto ROIC substrates, as shown in Figure 19 with no restrictions on pixel or array size and with a day cycle of production. In addition, the monolithic integration of CQD detectors into ROIC does not require any hybridization steps. Individual pixels are defined by the area of the metal pads arranged on the top of ROIC surface. To synthesize colloidal nanocrystals, wet chemistry techniques are used. Reagents are injected into a flask and, the desirable shape and size of nanocrystals are obtained by the control of reagent concentrations, ligand selection, and temperature. This so-called top-surface photodetector offers a 100% fill factor and is compatible with postprocessing at the top of complementary metal-oxide semiconductor (CMOS) electronics.

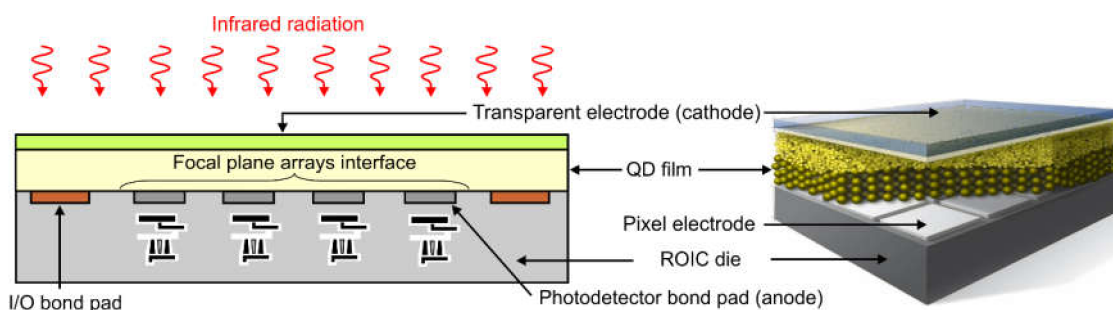


Figure 19. IR monolithic array structure based on CQDs.

The lead chalcogenides CQDs (primarily PbS) are the materials for SWIR photodetectors with detection to 2 μm . The peak can be adjusted using smaller dots by adding NIR bands to hyperspectral visible image sensors or using larger dots to include the InGaAs spectrum of image sensors [75]. From a performance standpoint, SWIR photodetectors based on PbS CQDs have reached detectivity, D^* comparable to commercial InGaAs photodiodes, with a values of $>10^{12}$ Jones at 300 K. HgTe CQDs have opened the MWIR spectral range. Detectivity, D^* between 10^{10} to 10^9 Jones at 5- μm was demonstrated for HgTe CQD devices while maintaining a fast response time at thermoelectric cooling temperatures. It is unlikely that CQD IR detectors will ever reach the performance of currently popular InGaAs, HgCdTe, InSb and T2SL photodiodes.

Recent demonstrations of low-cost SWIR and MWIR CQD imaging arrays have heightened the interest in these devices. For both PbS and HgTe CQD photodetectors integration in camera imaging have been demonstrated [76]. It is expected that the successful implementation of this new class of IR technology may match the broad impact of cheap CMOS cameras that are widely used today. First SWIR cameras built on CQD thin film photodiodes fabricated monolithically on silicon ROICs have been launched [77,78]. The Acuros camera has resolution 1920×1080 (2.1 megapixels, 15- μm pixel pitch) and uses 0.4 to 1.7 μm broadband spectral response [77]. The IMEC's prototype imager has resolution of 758×512 and 5 μm pixel pitch. The CQD photodiodes on silicon substrate reach an external QE above 60% at 940 nm wavelength, and above 20% at 1450 nm, allowing uncooled operation with dark current comparable to commercial InGaAs photodetectors [78].

At present, CQD cameras are used in newer applications that require high-definition low cost imaging on smaller pixels without extreme sensitivity. It can be predicted that increasing the dot size while maintaining a good mono-dispersion, carrier transport and QE will improve maintaining low noise levels. Due to continuous development of deposition and synthesis techniques, much higher performance will be reached in the future.

6.2. Present Status of CQD Photodiodes

Figure 7b compares the detectivity, D^* temperature dependence versus cut-off wavelength $\sim 5 \mu\text{m}$ for different material systems including commercially available HgCdTe and

HgTe CQD photodiodes. The gathered experimental data are also included. The estimated detectivity, D^* for CQD photodiodes are located below those for HgCdTe photodiodes. As is shown, at temperature above 200 K the theoretically predicted detectivity for HgCdTe photodiodes is limited by background. Rule 07 coincides well with theoretically predicted curve for Auger-suppressed p-on-n HgCdTe photodiode with doping concentration in active region 10^{15} cm^{-3} . As is marked in Section 3.3, at present stage of HgCdTe technology the doping concentration is almost two orders of magnitude lower (mid 10^{13} cm^{-3}).

All experimental data gathered in Figures 12 and 20 indicates on sub-BLIP photodetectors performance. Both figures also clearly show that the detectivity values of CQD photodetectors are inferior in comparison with HgCdTe photodiodes and are generally worse also in comparison with 2D material photodetectors. Moreover, the theoretical predictions indicate on possible further HgCdTe devices performance improvement after decreasing of i-doping level in P-i-N photodiodes. For doping level of $5 \times 10^{13} \text{ cm}^{-3}$ the photodiode performance can be limited by background radiation in spectral band above $3 \mu\text{m}$. It is shown that in this spectral region, the detectivity, D^* is not limited by detector itself, but by background photon noise at a level above 10^{10} Jones in LWIR range (above one order of magnitude above Rule 07).

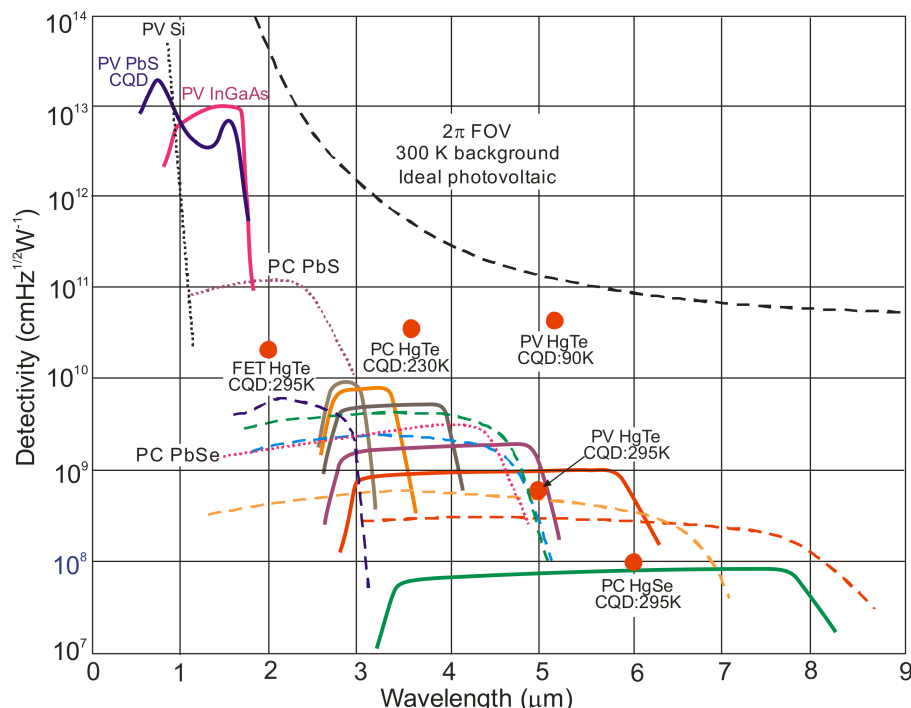


Figure 20. Room-temperature spectral detectivity curves of the commercially available photodetectors [PV Si and InGaAs, PC PbS and PbSe, HgCdTe photodiodes (solid lines reference [33])]. The experimental data for different types of CQD photodetectors are marked by dot points (reference [49,70,78–81]). Also, spectral detectivity of new emerging T2SL IB QCIPs are included [38]. PC—Photoconductor, PV—Photodiode.

7. Conclusions

In the last decade considerable progress in fabrication of SWIR and MWIR 2D material and CQD photodetectors has been demonstrated together with their integration into thermal imaging cameras. At current status of technology, the performance of both types of photodetectors is inferior in comparison with HgCdTe photodiodes. It seems that only PbS CQD photodetectors characterized by multicolor sensitivity and detectivity comparable to InGaAs detectors (which are currently the most common in commercial applications) have been located at the good position in IR material family at present time.

Discovery of graphene in 2004 gave a new impetus on technology development and investigations of 2D layered materials where their uncommon electronic and optical properties make them promising candidates for IR photodetectors. Despite spectacular demonstration of high detectivity like this achieved for black phosphorus layered photodetectors in MWIR spectral range [46] and noble TMD photodetectors like $\text{PdSe}_2/\text{MoS}_2$ heterojunction with record detectivity in LWIR range at room temperature [47], many challenges remain to be introduced to exploit the distinct advantages of these new materials. The prospect of commercialization of 2D material photodetectors depends on their large-scale integration with existing photonic and electronic platforms like CMOS technologies, high operability, spatial uniformity temporal stability, and affordability. Industry fabrication of devices is in the early stage of development and manufacturability.

In general, pristine narrow gap 2D materials are characterized by weak optical absorption and short carrier lifetime. Various ingenious approaches (electron trap layers, photogating effect with the graphene fast transfer channel) enhance sensitivity, however on the other side, degrade the electronic performance including carrier mobility. In this way high 2D material photodetector sensitivity collides with slow response time what seriously limits their practical applications.

In spite of sixty years development history of HgCdTe , its ultimate HOT performance limit has not been achieved. In order to achieve this goal, the doping concentration below $5 \times 10^{13} \text{ cm}^{-3}$ is required. This level of doping concentration has been recently achieved in fully-depleted HgCdTe FPAs by Teledyne Technologies.

At present stage of HgCdTe technology, the semiempirical rule Rule 07 (specified in 2007), widely popular in IR community as a reference for other technologies, was found not to fulfil primary expectations. In this paper, it was shown that the potential properties of HOT HgCdTe photodiodes operating above $3 \mu\text{m}$ guarantees achieving more than order of magnitude higher detectivity (above 10^{10} Jones) in comparison with value predicted by Rule 07, and this detectivity is limited by background. In this context it is rather difficult to compete 2D material and CQD photodetectors with HgCdTe photodiodes.

Author Contributions: Conceptualization, A.R., P.M.; writing—Original draft preparation, A.R., P.M., M.K. and W.H.; writing—Review and editing, A.R., P.M., M.K. and W.H.; visualization, A.R., P.M., M.K. and W.H.; supervision, A.R. and P.M.; project administration, A.R., P.M. and M.K.; funding acquisition, A.R., P.M. and M.K. All authors have read and agreed to the published version of the manuscript.

Funding: This research was funded by the Polish National Science Centre:, grant number OPUS-UMO-018/31/B/ST7/01541, HARMONIA-UMO-2018/30/M/ST7/00174, OPUS-UMO-2017/27/B/ST7/01507 and UMO-2019/33/B/ST7/00614.

Institutional Review Board Statement: Not applicable.

Informed Consent Statement: Not applicable.

Data Availability Statement: The data presented in this study are available on request from the corresponding author.

Conflicts of Interest: The authors declare no conflict of interest. The funders had no role in the design of the study; in the collection, analyses, or interpretation of data; in the writing of the manuscript, or in the decision to publish the results.

Abbreviations

2D	2 dimensional
3D	3 dimensional
α	The absorption coefficient
APD	Avalanche photodiode
bP	Black phosphorus
bP	Black phosphorus

bPAs	Black phosphorus-arsenic
c	Speed of light
C	Scene contrast
CMOS	Complementary metal-oxide semiconductor
CQD	Colloidal quantum dot
D [*]	Detectivity
FIR	Far infrared
FOV	Field-of-view
FPA	Focal plane arrays
g	Photoconductive gain
G	The thermal generation
h	Planck's constant
h-BN	Hexagonal boron nitride
HOT	High operating temperatures
IB QCIP	Interband quantum cascade infrared photodetectors
IR	Infrared radiation
J _{BLIP}	Background radiation current
J _{dark}	Dark current density
J _{dep}	Depletion current
J _{dif}	Diffusion current
λ	Wavelength
LWIR	Long wavelength infrared radiation
MBE	Molecular beam epitaxy
MWIR	Middle wavelength infrared radiation
MOCVD	Metalorganic chemical vapor deposition
NEDT	Noise equivalent difference temperature
n	Electron concentration
n _i	Intrinsic carrier concentration
NIR	Near infrared
p	Hole concentration
PC	Photoconductor
PEM	Photoelectromagnetic
PV	Photodiode
R _i	Current responsivity
q	The electron charge
QE	Quantum efficiency
QD	Quantum dot
QDIP	Quantum dot infrared photodetectors
QWIP	Quantum well infrared photodetectors
R _{0A}	Dynamic resistance area product
ROIC	Readout integration circuits
SRH	Shockley-Read-Hall
SWaP	Size, weight, and power consumption
SWIR	Short wavelength infrared radiation
T2SLs	Type-II superlattices
THz	Terahertz
TMD	Transition metal dichalcogenide
τ _{A1}	Auger 1 lifetime
τ _{AI}	Intrinsic Auger 1 lifetime
τ _{int}	Integration time
τ _{po}	Specific SRH lifetimes
τ _{SRH}	SRH lifetime
UV	Ultraviolet
vdW	van der Waals
Φ _B	Background flux

References

- Iwert, O.; Delabrea, O. The challenge of highly curved monolithic imaging detectors. *Proc. SPIE* **2010**, *7742*, 774227.
- Jeong, K.-H.; Kim, J.; Lee, L.P. Biologically inspired artificial compound eyes. *Science* **2006**, *312*, 557–561. [CrossRef] [PubMed]
- Song, Y.M.; Xie, Y.; Malyarchuk, V.; Xiao, J.; Jung, I.; Choi, K.-J.; Liu, Z.; Park, H.; Lu, C.; Kim, R.H.; et al. Digital cameras with designs inspired by the arthropod eye. *Nature* **2013**, *497*, 95–99. [CrossRef] [PubMed]
- Tang, X.; Ackerman, M.M.; Guyot-Sionnest, P. Colloidal quantum dots based infrared electronic eyes for multispectral imaging. *Proc. SPIE* **2019**, *11088*, 1108803.
- Lu, Q.; Liu, W.; Wang, X. 2-D Material-Based Photodetectors on Flexible Substrates. In *Inorganic Flexible Optoelectronics: Materials and Applications*; Ma, Z., Liu, D., Eds.; Wiley-VCH Verlag: Weinheim, Germany, 2019; pp. 117–142.
- Piotrowski, J.; Galus, W.; Grudzień, M. Near room temperature IR photodetectors. *Infrared Phys. Technol.* **1991**, *31*, 1–48. [CrossRef]
- Piotrowski, J.; Rogalski, A. Photoelectromagnetic, Magnetoconcentration and Dember Infrared Detectors. In *Narrow-Gap II–VI Compounds and Electromagnetic Applications*; Capper, P., Ed.; Chapman & Hall: London, UK, 1997; pp. 506–525.
- Piotrowski, J.; Rogalski, A. Uncooled long wavelength infrared photon detectors. *Infrared Phys. Technol.* **2004**, *46*, 115–131. [CrossRef]
- Piotrowski, J.; Rogalski, A. *High-Operating-Temperature Infrared Photodetectors*; SPIE Press: Bellingham, WA, USA, 2007.
- Piotrowski, J.; Pawluczyk, J.; Piotrowski, A.; Gawron, W.; Romanis, M.; Kłos, K. Uncooled MWIR and LWIR photodetectors in Poland. *Opto-Electron. Rev.* **2010**, *18*, 318–327. [CrossRef]
- Rogalski, A.; Kopytko, M.; Martyniuk, P. *Antimonide-Based Infrared Detectors. A New Perspective*; SPIE Press: Bellingham, WA, USA, 2018.
- Rogalski, A.; Kopytko, M.; Martyniuk, P. Two-dimensional infrared and terahertz detectors: Outlook and status. *Appl. Phys. Rev.* **2019**, *6*, 021316. [CrossRef]
- Guyot-Sionnest, P.; Ackerman, M.M.; Tang, X. Colloidal quantum dots for infrared detection beyond silicon. *J. Chem. Phys.* **2019**, *151*, 60901. [CrossRef]
- Elliott, C.T.; Gordon, N.T.; White, A.M. Towards background-limited, room-temperature, infrared photon detectors in the 3–13 μm wavelength range. *Appl. Phys. Lett.* **1999**, *74*, 2881–2883. [CrossRef]
- Piotrowski, J.; Rogalski, A. Comment on “Temperature limits on infrared detectivities of InAs/In_xGa_{1-x}Sb superlattices and bulk Hg_{1-x}Cd_xTe”. *J. Appl. Phys.* **1996**, *80*, 2542–2544. [CrossRef]
- Rogalski, A. *Infrared and Terahertz Detectors*; CRC Press: Boca Raton, FL, USA, 2019.
- Robinson, J.; Kinch, M.; Marquis, M.; Littlejohn, D.; Jeppson, K. Case for small pixels: System perspective and FPA challenge. *Proc. SPIE* **2014**, *9100*, 910001.
- Rogalski, A.; Martyniuk, P.; Kopytko, M. Challenges of small-pixel infrared detectors: A review. *Rep. Prog. Phys.* **2016**, *79*, 046501-1–42. [CrossRef] [PubMed]
- Holst, G.C.; Lomheim, T.C. *CMOS/CCD Sensors and Camera Systems*; JCD Publishing and SPIE Press: Winter Park, CO, USA, 2007.
- Kinch, M.A. *State-of-the-Art Infrared Detector Technology*; SPIE Press: Bellingham, WA, USA, 2014.
- Holst, G.C.; Driggers, R.G. Small detectors in infrared system design. *Opt. Eng.* **2012**, *51*, 96401. [CrossRef]
- Tennant, W.E.; Lee, D.; Zandian, M.; Piquette, E.; Carmody, M. MBE HgCdTe technology: A very general solution to IR detection, described by ‘Rule 07’, a very convenient heuristic. *J. Electron. Mater.* **2008**, *37*, 1406–1410. [CrossRef]
- Kinch, M.S.; Aqariden, F.; Chandra, D.; Liao, P.-K.; Schaake, H.F.; Shih, H.D. Minority carrier lifetime in p-HgCdTe. *J. Electron. Mater.* **2005**, *34*, 880–884. [CrossRef]
- Gravrand, O.; Rothman, J.; Delacourt, B.; Boulard, F.; Lobre, C.; Ballet, P.H.; Santialler, J.L.; Cervera, C.; Brellier, D.; Pere-Laperne, N.; et al. Shockley-Read-Hall lifetime study and implication in HgCdTe photodiodes for IR detection. *J. Electron. Mater.* **2018**, *47*, 5680–5690. [CrossRef]
- Lee, D.; Dreiske, P.; Ellsworth, J.; Cottier, R.; Chen, A.; Tallarico, S.; Yulius, A.; Carmody, M.; Piquette, E.; Zandian, M.; et al. Law 19—The ultimate photodiode performance metric. Extended Abstracts. In Proceedings of the 2019 U.S. Workshop on the Physics and Chemistry of II–VI Materials, Chicago, IL, USA, 18–21 November 2019; pp. 13–15.
- Lee, D.; Carmody, M.; Piquette, E.; Dreiske, P.; Chen, A.; Yulius, A.; Edwall, D.; Bhargava, S.; Zandian, M.; Tennant, W.E. High-operating temperature HgCdTe: A vision for the near future. *J. Electron. Mater.* **2016**, *45*, 4587–4595. [CrossRef]
- Kopytko, M.; Józwikowski, K.; Martyniuk, P.; Rogalski, A. Photon recycling effect in small pixel p-i-n HgCdTe long wavelength infrared photodiodes. *Infrared Phys. Technol.* **2019**, *97*, 38–42. [CrossRef]
- Rhiger, D.R. Performance comparison of long-wavelength infrared type II superlattice devices with HgCdTe. *J. Elect. Mater.* **2011**, *40*, 1815–1822. [CrossRef]
- Klipstein, P.C.; Avnon, E.; Azulai, D.; Benny, Y.; Fraenkel, R.; Glzman, A.; Hojman, E.; Klin, O.; Krasovitsky, L.; Langof, L.; et al. Type II superlattice technology for LWIR detectors. *Proc. SPIE* **2016**, *9819*, 98190T.
- Huang, W.; Rassela, S.M.S.; Li, L.; Massengale, J.A.; Yang, R.Q.; Mishima, T.D.; Santos, M.B. A unified figure of merit for interband and intersubband cascade devices. *Infrared Phys. Technol.* **2019**, *96*, 298–301. [CrossRef]
- Rogalski, A.; Ciupa, R. Performance limitation of short wavelength infrared InGaAs and HgCdTe photodiodes. *J. Electron. Mater.* **1999**, *28*, 630–636. [CrossRef]
- Rogalski, A.; Kopytko, M.; Martyniuk, P. Performance prediction of p-i-n HgCdTe long-wavelength infrared HOT photodiodes. *Appl. Optics* **2018**, *57*, D11–D19. [CrossRef] [PubMed]

33. Available online: <https://vigo.com.pl/wp-content/uploads/2017/06/VIGO-Catalogue.pdf> (accessed on 30 October 2020).
34. HOT MCT Detectors. Available online: <http://www.teledynejudson.com/> (accessed on 30 October 2020).
35. Ashley, T.; Elliott, C.T. Non-equilibrium mode of operation for infrared detection. *Electron. Lett.* **1985**, *21*, 451–452. [CrossRef]
36. Elliott, C.T. Non-equilibrium mode of operation of narrow-gap semiconductor devices. *Semicond. Sci. Technol.* **1990**, *5*, S30–S37. [CrossRef]
37. Gomez, A.; Carras, M.; Nedelcu, A.; Costard, E.; Marcadet, X.; Berger, V. Advantages of quantum cascade detectors. *Proc. SPIE* **2008**, *6900*, 69000J.
38. Rogalski, A.; Martyniuk, P.; Kopytko, M. Type-II superlattice photodetectors versus HgCdTe photodiodes. *Prog. Quantum Electron.* **2019**, *68*, 100228. [CrossRef]
39. Huang, W.; Li, L.; Lei, L.; Massengale, J.A.; Yang, R.Q.; Mishima, T.D.; Santos, M.B. Electrical gain in interband cascade infrared photodetectors. *J. Appl. Phys.* **2018**, *123*, 113104. [CrossRef]
40. Hinkey, R.T.; Yang, R.Q. Theory of multiple-stage interband photovoltaic devices and ultimate performance limit comparison of multiple-stage and single-stage interband infrared detectors. *J. Appl. Phys.* **2013**, *114*, 104506. [CrossRef]
41. Huang, W.; Lei, L.; Li, L.; Massengale, J.A.; Yang, R.Q.; Mishima, T.D.; Santos, M.B. Current-matching versus non-current-matching in long wavelength interband cascade infrared photodetectors. *J. Appl. Phys.* **2017**, *122*, 83102. [CrossRef]
42. Lei, L.; Li, L.; Lotfi, H.; Ye, H.; Yang, R.Q.; Mishima, T.D.; Santos, M.B.; Johnson, M.B. Mid wavelength interband cascade infrared photodetectors with superlattice absorbers and gain. *Opt. Eng.* **2018**, *57*, 11006.
43. Long, M.; Gao, A.; Wang, P.; Xia, H.; Ott, C.; Pan, C.; Fu, Y.; Liu, E.; Chen, X.; Lu, W.; et al. Room temperature high-detectivity mid-infrared photodetectors based on black arsenic phosphorus. *Sci. Adv.* **2017**, *3*, e1700589. [CrossRef] [PubMed]
44. Du, S.; Lu, W.; Ali, A.; Zhao, P.; Shehzad, K.; Guo, H.; Ma, L.; Liu, X.; Pi, X.; Wang, P.; et al. A broadband fluorographene photodetector. *Adv. Mater.* **2017**, *29*, 1700463. [CrossRef]
45. Ye, L.; Wang, P.; Luo, W.; Gong, F.; Liao, L.; Liu, T.; Tong, L.; Zang, J.; Xu, J.; Hu, W. Highly polarization sensitive infrared photodetector based on black phosphorus-on-WSe₂ photogate vertical heterostructure. *Nano Energy* **2017**, *37*, 53–60. [CrossRef]
46. Amani, M.; Regan, E.; Bullock, J.; Ahn, G.H.; Javey, A. Mid-wave infrared photoconductors based on black phosphorus-arsenic alloys. *ACS Nano* **2017**, *11*, 11724–11731. [CrossRef]
47. Long, M.; Wang, Y.; Wang, P.; Zhou, X.; Xia, H.; Luo, C.; Huang, S.; Zhang, G.; Yan, H.; Fan, Z.; et al. Palladium diselenide long-wavelength infrared photodetector with high sensitivity and stability. *ACS Nano* **2019**, *13*, 2511–2519. [CrossRef]
48. Yu, X.; Yu, P.; Wu, D.; Singh, B.; Zeng, Q.; Lin, H.; Zhou, W.; Lin, J.; Suenaga, K.; Liu, Z.; et al. Atomically thin noble metal dichalcogenide: A broadband mid-infrared semiconductor. *Nat. Commun.* **2018**, *9*, 1545. [CrossRef]
49. Konstantatos, G. Current status and technological prospect of photodetectors based on two-dimensional materials. *Nat. Commun.* **2018**, *9*, 5266. [CrossRef]
50. Konstantatos, G.; Sargent, E.H. Solution-processed quantum dot photodetectors. *Proc. IEEE* **2009**, *97*, 1666–1683. [CrossRef]
51. Konstantatos, G.; Badioli, M.; Gaudreau, L.; Osmond, J.; Bernechea, M.; Garcia de Arquer, F.P.; Gatti, F.; Koppens, F.H.L. Hybrid graphene-quantum dot phototransistors with ultrahigh gain. *Nat. Nanotechnol.* **2012**, *7*, 363–368. [CrossRef] [PubMed]
52. Morgan, H.; Rout, C.S.; Late, D.J. (Eds.) *Fundamentals and Sensing Applications of 2D Materials*; Woodhead Publishing Series in Electronic and Optical Materials; United Kingdom Elsevier: London, UK, 2019.
53. Nicolosi, V.; Chhowalla, M.; Kanatzidis, M.G.; Strano, M.S.; Coleman, J.N. Liquid exfoliation of layered materials. *Science* **2013**, *340*, 1226419. [CrossRef]
54. Yang, Z.; Dou, J.; Wang, M. Graphene, transition metal dichalcogenides, and perovskite photodetectors. In *Two-Dimensional Materials for Photodetector*; IntechOpen: Rijeka, Croatia, 2018. [CrossRef]
55. Wang, X.; Sun, Y.; Liu, K. Chemical and structural stability of 2D layered materials. *2D Mater.* **2019**, *6*, 42001. [CrossRef]
56. Ling, X.; Wang, H.; Huang, S.; Xia, F.; Dresselhaus, M.S. The renaissance of black phosphorus. *Proc. Natl. Acad. Sci. USA* **2015**, *112*, 4523–4530. [CrossRef] [PubMed]
57. Wang, P.; Xia, H.; Li, Q.; Wang, F.; Zhang, L.; Li, T.; Martyniuk, P.; Rogalski, A.; Hu, W. Sensing infrared photons at room temperature: From bulk materials to atomic layers. *Small* **2019**, *46*, 1904396. [CrossRef]
58. Currie, M. *Applications of Graphene to Photonics*; Report NRL/MR/5650-14-9550; Naval Research Laboratory: Washington, DC, USA, 2014.
59. Rogalski, A.; Kopytko, M.; Martyniuk, P. 2D material infrared and terahertz detectors: status and outlook. *Opto-Electron. Rev.* **2020**, *28*, 107–154.
60. Cakmakyapan, S.; Lu, P.K.; Navabi, A.; Jarrahi, M. Gold-patched graphene nano-stripes for high-responsivity and ultrafast photodetection from the visible to infrared regime. *Light Sci. Appl.* **2018**, *7*, 20. [CrossRef]
61. Wang, F.; Wang, Z.; Yin, L.; Cheng, R.; Wang, J.; Wen, Y.; Shifa, T.A.; Wang, F.; Zhang, Y.; Zhan, X.; et al. 2D library beyond graphene and transition metal dichalcogenides: A focus on photodetection. *Chem. Soc. Rev.* **2018**, *47*, 6296–6341. [CrossRef]
62. Buscema, M.; Island, J.O.; Groenendijk, D.J.; Blanter, S.I.; Steele, G.A.; Van der Zant, H.S.J.; Castellanos-Gomez, A. Photocurrent generation with two-dimensional van der Waals semiconductor. *Chem. Soc. Rev.* **2015**, *44*, 3691–3718. [CrossRef]
63. Wang, J.; Fang, H.; Wang, X.; Chen, X.; Lu, W.; Hu, W. Recent progress on localized field enhanced two-dimensional material photodetectors from ultraviolet-visible to infrared. *Small* **2017**, *13*, 1700894. [CrossRef]
64. Long, M.; Wang, P.; Fang, H.; Hu, W. Progress, challenges, and opportunities for 2D material based photodetectors. *Adv. Funct. Mater.* **2018**, *29*, 1803807. [CrossRef]

65. Xu, Y.; Shi, Z.; Shi, X.; Zhang, K.; Zhang, H. Recent progress in black phosphorus and black-phosphorus-analogue materials: Properties, synthesis and applications. *Nanoscale* **2019**, *11*, 14491–14527. [CrossRef] [PubMed]
66. Lee, D.; Dreiske, P.; Ellsworth, J.; Cottier, R.; Chen, A.; Tallarico, S.; Barr, H.; Tcheou, H.; Julius, A.; Carmody, M.; et al. Performance of MWIR and LWIR fully-depleted HgCdTe FPAs. Extended Abstracts. In Proceedings of the 2019 U.S. Workshop on the Physics and Chemistry of II-VI Materials, Chicago, IL, USA, 18–21 November 2019; pp. 189–190.
67. Martyniuk, P.; Rogalski, A. Comparison of performance of quantum dot and other types infrared photodetectors. *Proc. SPIE* **2008**, *6940*, 694004.
68. Stiff-Roberts, A.D. Quantum-dot infrared photodetectors: A review. *J. Nanophotonics* **2009**, *3*, 31607. [CrossRef]
69. Ginger, D.S.; Greenham, N.C. Photoinduced electron transfer from conjugated polymers to CdSe nanocrystals. *Phys. Rev. B* **1999**, *59*, 10622–10629. [CrossRef]
70. Garcia de Arquer, F.P.; Armin, A.; Meredith, P.; Sargent, E.H. Solution-processed semiconductors for next-generation photodetectors. *Nat. Rev. Mater.* **2017**, *2*, 16100. [CrossRef]
71. Guyot-Sionnest, P.; Roberts, J.A. Background limited mid-infrared photodetection with photovoltaic HgTe colloidal quantum dots. *Appl. Phys. Lett.* **2015**, *107*, 91115. [CrossRef]
72. Buurma, C.; Ciani, A.J.; Pimpinella, R.E.; Feldman, J.S.; Grein, C.H.; Guyot-Sionnes, P. Advances in HgTe colloidal quantum dots for infrared detectors. *J. Electron. Mater.* **2017**, *46*, 6685–6688. [CrossRef]
73. De Iacovo, A.; Venettacci, C.; Colace, L.; Scopa, L.; Foglia, S. PbS colloidal quantum dot photodetectors operating in the near infrared. *Sci. Rep.* **2016**, *6*, 37913. [CrossRef]
74. Thambidurai, M.; Jjang, Y.; Shapiro, A.; Yuan, G.; Xiaonan, H.; Xuechao, Y.; Wang, G.J.; Lifshitz, E.; Demir, H.V.; Dang, C. High performance infrared photodetectors up to 2.8 μm wavelength based on lead selenide colloidal quantum dots. *Opt. Mater. Express* **2017**, *7*, 2336. [CrossRef]
75. Malinowski, P.E.; Georgitzikis, E.; Maes, J.; Vamvaka, I.; Fazzica, F.; Van Olmen, J.; De Moor, P.; Heremans, P.; Hens, Z.; Cheyns, D. Thin-film quantum dot photodiode for monolithic infrared image sensors. *Sensors* **2017**, *17*, 2867. [CrossRef] [PubMed]
76. Hafiz, S.B.; Scimeca, M.; Sahu, A.; Ko, D.-K. Colloidal quantum dots for thermal infrared sensing and imaging. *Nano Converg.* **2019**, *6*, 7. [CrossRef] [PubMed]
77. Available online: https://ibv.vdma.org/documents/256550/27019077/2018-11-07_Stage1_1030_SWIR+Vision+Systems.pdf/ (accessed on 30 October 2020).
78. Available online: <https://optics.org/news/10/10/38> (accessed on 30 October 2020).
79. Lhuillier, E.; Guyot-Sionnest, P. Recent progress in mid infrared nanocrystal optoelectronics. *IEEE J. Sel. Top. Quantum Electron.* **2017**, *23*, 6000208. [CrossRef]
80. Chen, M.; Lu, H.; Abdelazim, N.M.; Zhu, Y.; Wang, Z.; Ren, W.; Kershaw, S.V.; Rogach, A.L.; Zhao, N. Mercury telluride quantum dot based phototransistor enabling high-sensitivity room-temperature photodetection at 2000 nm. *ACS Nano* **2017**, *11*, 5614–5622. [CrossRef] [PubMed]
81. Livache, C.; Martinez, B.; Goubet, N.; Ramade, J.; Lhuillier, E. Road map for nanocrystal based infrared photodetectors. *Front. Chem.* **2018**, *6*, 575. [CrossRef] [PubMed]